

**Explicit Structure-Preserving Geometric Particle-in-Cell
Algorithm in Curvilinear Orthogonal Coordinate Systems and Its
Applications to Whole-Device 6D Kinetic Simulations of
Tokamak Physics**

Jianyuan Xiao^{1,*} and Hong Qin^{2,†}

¹*School of Nuclear Science and Technology,*

University of Science and Technology of China, Hefei, 230026, China

²*Plasma Physics Laboratory, Princeton University, Princeton, NJ 08543, U.S.A.*

arXiv:2004.08150v4 [physics.plasm-ph] 10 Mar 2021

Abstract

Explicit structure-preserving geometric Particle-in-Cell (PIC) algorithm in curvilinear orthogonal coordinate systems is developed. The work reported represents a further development of the structure-preserving geometric PIC algorithm [1–12], achieving the goal of practical applications in magnetic fusion research. The algorithm is constructed by discretizing the field theory for the system of charged particles and electromagnetic field using Whitney forms, discrete exterior calculus, and explicit non-canonical symplectic integration. In addition to the truncated infinitely dimensional symplectic structure, the algorithm preserves exactly many important physical symmetries and conservation laws, such as local energy conservation, gauge symmetry and the corresponding local charge conservation. As a result, the algorithm possesses the long-term accuracy and fidelity required for first-principles-based simulations of the multiscale tokamak physics. The algorithm has been implemented in the *SymPIC* code, which is designed for high-efficiency massively-parallel PIC simulations in modern clusters. The code has been applied to carry out whole-device 6D kinetic simulation studies of tokamak physics. A self-consistent kinetic steady state for fusion plasma in the tokamak geometry is numerically found with a predominately diagonal and anisotropic pressure tensor. The state also admits a steady-state sub-sonic ion flow in the range of 10 km/s, agreeing with experimental observations [13, 14] and analytical calculations [15, 16]. Kinetic ballooning instability in the self-consistent kinetic steady state is simulated. It shows that high- n ballooning modes have larger growth rates than low- n global modes, and in the nonlinear phase the modes saturate approximately in 5 ion transit times at the 2% level by the $E \times B$ flow generated by the instability. These results are consistent with early [17, 18] and recent [19] electromagnetic gyrokinetic simulations.

* xiaojy@ustc.edu.cn

† hongqin@princeton.edu

I. INTRODUCTION

Six Dimensional (6D) Particle-In-Cell (PIC) simulation is a powerful tool for studying complex collective dynamics in plasmas [20–22]. However, as a first-principles-based numerical method, 6D PIC simulation has not been employed to study the dynamical behavior experimentally observed in magnetic fusion plasmas, mainly due to the multiscale nature of the physics involved. The technical difficulties are two-fold. First, the span of space-time scales of magnetic fusion plasmas is enormous, and numerically resolving these space-time scales demands computation hardware that did not exist until very recently. Secondly, even if unlimited computing resource exists, the standard 6D PIC algorithms do not possess the long-term accuracy and fidelity required for first-principles-based simulations of magnetic fusion plasmas. For example, the most commonly used 6D PIC scheme is the Boris-Yee scheme, which solves the electromagnetic fields using the Yee-FDTD [23] method and advances particles' position and velocity by the Boris algorithm [24]. Even though both Yee-FDTD method [25] and the Boris algorithm [26–31] themselves do have good conservative properties, their combination in PIC methods does not [21, 22, 32]. Numerical errors thus accumulate coherently during simulations and long-term simulation results are not trustworthy.

Recent advances in super-computers [33] have made 6D PIC simulation of magnetic fusion plasmas possible in terms of hardware. On the other hand, much needed now is modern 6D PIC algorithms that can harness the rapidly increasing power of computation hardware. A family of such new 6D PIC algorithms [1–12] has been developed recently. Relative to the conventional PIC methods, two unique properties characterize these new PIC algorithms: the space-time discretization is designed using modern geometric methods, such as discrete manifold and symplectic integration, and the algorithms preserve exactly many important physical symmetries and conservation laws in a discrete sense. For this reason, these algorithms are called structure-preserving geometric PIC algorithms. The long-term accuracy and fidelity of these algorithms have been studied and documented by different research groups [4, 9, 34–43].

Discrete symplectic structure and symplectic integration are two of the main features of the structure-preserving geometric PIC algorithms. Up to now, the only explicit symplectic integrator for the non-canonical symplectic structure of the discrete or continuous Vlasov-

Maxwell system is the splitting method developed in Ref. [6], which splits the dynamics symplectically into one-way decoupled Cartesian components. The requirement of the Cartesian coordinate system creates a hurdle for applications in magnetic fusion plasmas, for which cylindrical or toroidal coordinate systems are more convenient. Most simulation codes, such as GTC [44, 45], XGC [46, 47] and GEM [48–50] adopted curvilinear coordinate systems. In the present study, we extend the structure-preserving geometric PIC algorithm to arbitrary curvilinear orthogonal coordinate systems, in particular, to the cylindrical coordinate system for applications in tokamak physics. We show that when a sufficient condition (40) is satisfied, which is the case for the cylindrical mesh, the structure-preserving PIC algorithm can be made explicitly solvable and high-order. For easy implementation and presentation, we first present the algorithm as a discrete field theory [51–56] specified by a Lagrangian discretized in both space and time. It is then reformulated using a generalized version of the discrete Poisson bracket developed in Ref. [4] and an associated explicit symplectic splitting algorithm, which generalizes the original algorithm designed in Ref. [6] in the Cartesian coordinate system. In particular, the technique utilizing the one-way decoupling of dynamic components is generalized to arbitrary curvilinear orthogonal coordinate systems satisfying condition (40).

The algorithm has been implemented in the the *SymPIC* code and applied to carry out whole-device 6D kinetic PIC simulations of plasma physics in a small tokamak with similar machine parameters as the Alcator C-Mod [57, 58]. We numerically study two topics: self-consistent kinetic steady state in the tokamak geometry and kinetic ballooning instability in the edge. Simulation shows that when plasma reaches a self-consistent kinetic steady state, the pressure tensor is diagonal, anisotropic in 3D, but isotropic in the poloidal plane. A subsonic ion flow in the range of 10km/s exists, which agrees with experimental observations [13, 14] and theoretical calculations [15, 16]. In the self-consistent kinetic steady state, it is found that large- n kinetic ballooning modes grow faster than low- n global modes, and the instability saturates nonlinearly at the 2% level by the $E \times B$ flow generated by the instability. These results qualitatively agree with previous simulations by electromagnetic gyrokinetic codes [17–19].

Because the algorithm is based on first-principles of physics and constructed in general geometries, the whole-device 6D kinetic simulation capability developed is applicable to other fusion devices and concepts as well, including stellarators, field reserve configurations

and inertial confinement. It is also worthwhile to mention that the structure-preserving geometric discretization technique developed for the 6D electromagnetic PIC simulations can be applied to other systems as well, including ideal two-fluid systems [59] and magnetohydrodynamics [60–64]. Structure-preserving geometric algorithms have also been developed for the Schrödinger-Maxwell [65] system, the Klein-Gordon-Maxwell system [66–69], and the Dirac-Maxwell system [70], which have important applications in high energy density physics. Another noteworthy development is the metriplectic particle-in-cell integrators for the Landau collision operator [71]. Recently, a field theory and a corresponding 6D structure-preserving geometric PIC algorithm were established for low-frequency electrostatic perturbations in magnetized plasmas with adiabatic electrons [12]. The long-term accuracy and fidelity of the algorithm enabled the simulation study of electrostatic drift wave turbulence and transport using a 6D PIC method with adiabatic electrons.

The paper is organized as follows. In Sec. II we develop the explicit structure-preserving geometric PIC scheme in arbitrary orthogonal coordinate systems, and the algorithm in a cylindrical mesh is implemented in the *SymPIC* code. In Sec. III, the code is applied to carry out whole-device 6D kinetic PIC simulations of tokamak physics.

II. EXPLICIT STRUCTURE-PRESERVING GEOMETRIC PIC ALGORITHM IN CURVILINEAR ORTHOGONAL COORDINATE SYSTEMS

A. The basic principles of structure-preserving geometric PIC algorithm

The procedure of designing a structure-preserving geometric PIC algorithm starts from a field theory, or variational principle, for the system of charged particles and electromagnetic field. Instead of discretizing the corresponding Vlasov-Maxwell equations, the variational principle is discretized.

For spatial discretization of the electromagnetic field, discrete exterior calculus [72, 73] is adopted. As indicated by its name, a PIC algorithm contains two components not found in other simulation methods: charge and current deposition from particles to grid points, and field interpolation from grid points to particles. Note that these two components are independent from the field solver, e.g., the Yee-FDTD method, and the particle pusher, e.g., the Boris algorithm. In conventional PIC algorithms [20–22], the function of charge and

current deposition and the function of field interpolation are implemented using intuitive techniques without fundamental guiding principles other than the consistency requirement. It was found [1, 2, 11] that a systematic method to realize these two functions is to apply the Whitney interpolation (differential) forms [74] and their high-order generalizations [4] on the discrete Lagrangian.

The application of Whitney forms is a key technology for achieving the goal of preserving geometric structures and conservation laws. It stipulates from first principles how charge and current deposition and field interpolation should be performed [1–12]. It also enabled the derivation of the discrete non-canonical symplectic structure and Poisson bracket for the charged particle-electromagnetic field system [4]. At the continuous limit when the size of the space-time grid approaches zero, the discrete non-canonical Poisson bracket reduces to the Morrison-Marsden-Weinstein (MMW) bracket for the Vlasov-Maxwell equations [34, 75–78] (The MMW bracket was also independently discovered by Iwinski and Turski [79]). To derive the discrete Poisson bracket, Whitney forms and their high-order generalizations are adopted for the purpose of geometric spatial discretization of the field Lagrangian density as an 1-form in the phase space of the charged particle-electromagnetic field system, whose exterior derivative automatically generates a discrete non-canonical symplectic structure and consequently a Poisson bracket. As a different approach, He et al. [8] and Kraus et al. [9] used the method of finite element exterior calculus to discretize the MMW bracket directly, and verified explicitly that the discretized bracket satisfies the Jacobi identity through lengthy calculations, in order for the discretized bracket to be a legitimate Poisson bracket. If one chooses to discretize the MMW bracket directly [39, 40], such verification is necessary because there are other discretizations of the MMW bracket which satisfy the numerical consistency requirement but not the Jacobi identity. On the other hand, the discrete Poisson bracket in Ref. [4] was not a discretization of the MMW bracket. It was derived from the spatially discretized 1-form using Whitney forms and is naturally endowed with a symplectic structure and Poisson bracket, and reduces to the MMW bracket in the continuous limit. The advantage of this discrete Poisson bracket in this respect demonstrates the power of Whitney forms in the design of structure-preserving geometric PIC algorithms.

To numerically integrate a Hamiltonian or Poisson system for the purpose of studying multiscale physics, symplectic integrators are necessities. Without an effective symplectic integrator, a symplectic or Poisson structure is not beneficial in terms of providing a better

algorithm with long-term accuracy and fidelity. However, essentially all known symplectic integrators are designed for canonical Hamiltonian systems [51–55, 80–99], except for recent investigations on non-canonical symplectic integrators [100–113] for charged particle dynamics in a given electromagnetic field. Generic symplectic integrators for non-canonical symplectic systems are not known to exist. Fortunately, a high-order explicit symplectic integrator for the MMW bracket was discovered [6] using a splitting technique in the Cartesian coordinate system. The validity of this explicit non-canonical symplectic splitting method is built upon the serendipitous one-way decoupling of the dynamic components of the particle-field system in the Cartesian coordinate system. It’s immediately realized [4] that this explicit non-canonical symplectic splitting applies to the discrete non-canonical Poisson bracket without modification for the charged particle-electromagnetic field system. This method was also adopted in Refs. [8] and [9] to integrate the discretized MMW bracket using finite element exterior calculus. See also Refs. [114] and [115] for early effort for developing symplectic splitting method for the Vlasov-Maxwell system. It was recently proven [11] that the discrete non-canonical Poisson bracket [4] and the explicit non-canonical symplectic splitting algorithm [6] can be equivalently formulated as a discrete field theory [56] using a Lagrangian discretized in both space and time.

The geometric discretization of the field theory for the system of charged particles and electromagnetic field using Whitney forms [2, 4, 74], discrete exterior calculus [72, 73], and explicit non-canonical symplectic integration [4, 6] results in a PIC algorithm preserving many important physical symmetries and conservation laws. In addition to the truncated infinitely dimensional symplectic structure, the algorithms preserves exactly the local conservation laws for charge [1, 2, 11] and energy [10]. It was shown that the discrete local charge conservation law is a natural consequence of the discrete gauge symmetry admitted by the system [1, 2, 11, 116]. The correspondence between discrete space-time translation symmetry [117, 118] and discrete local energy-momentum conservation law has also been established for the Maxwell system [119].

As mentioned in Sec.I, the goal of this section is to extend the explicit structure-preserving geometric particle-in-cell algorithm, especially the discrete non-canonical Poisson bracket [4] and the explicit non-canonical symplectic splitting algorithm [6], from the Cartesian coordinate systems to curvilinear orthogonal coordinate systems that are suitable for the tokamak geometry.

B. Field theory of the particle-field system in curvilinear orthogonal coordinate systems

We start from the action integral of the system of charged particles and electromagnetic field. In a curvilinear orthogonal coordinate system (x_1, x_2, x_3) with line element

$$ds^2 = h_1(x_1, x_2, x_3)^2 dx_1^2 + h_2(x_1, x_2, x_3)^2 dx_2^2 + h_3(x_1, x_2, x_3)^2 dx_3^2, \quad (1)$$

the action integral of the system is

$$\begin{aligned} \mathcal{A}[\mathbf{x}_{sp}, \dot{\mathbf{x}}_{sp}, \mathbf{A}, \phi] = & \int dt \sum_{s,p} (L_{sp}(m_s, \mathbf{v}_{sp}) + q_s (\mathbf{v}_{sp} \cdot \mathbf{A}(\mathbf{x}_{sp}, t) - \phi(\mathbf{x}_{sp}, t))) \\ & + \int dV dt \frac{1}{2} \left((-\dot{\mathbf{A}}(\mathbf{x}, t) - \nabla \phi(\mathbf{x}, t))^2 - (\nabla \times \mathbf{A}(\mathbf{x}, t))^2 \right), \quad (2) \end{aligned}$$

where $\mathbf{x} = [x_1, x_2, x_3]$ and $dV = |h_1(\mathbf{x}) h_2(\mathbf{x}) h_3(\mathbf{x})| dx_1 dx_2 dx_3$. In this coordinate system, the position and velocity of the p -th particle of species s are $\mathbf{x}_{sp} = [x_{sp1}, x_{sp2}, x_{sp3}]$ and $\mathbf{v}_{sp} = [\dot{x}_{sp1} h_1(\mathbf{x}_{sp}), \dot{x}_{sp2} h_2(\mathbf{x}_{sp}), \dot{x}_{sp3} h_3(\mathbf{x}_{sp})]$. L_{sp} is the free Lagrangian for the p -th particle of species s . For the non-relativistic case $L_{sp} = m_s |\mathbf{v}_{sp}|^2 / 2$, and for the relativistic case $L_{sp} = -m_s \sqrt{1 - |\mathbf{v}_{sp}|^2}$. Here, we set both permittivity ϵ_0 and permeability μ_0 in the vacuum to 1 to simplify the notation. The evolution of this system is governed by the variational principle,

$$\frac{\delta \mathcal{A}}{\delta \mathbf{A}} = 0, \quad (3)$$

$$\frac{\delta \mathcal{A}}{\delta \phi} = 0, \quad (4)$$

$$\frac{\delta \mathcal{A}}{\delta \mathbf{x}_{sp}} = 0. \quad (5)$$

It can be verified that Eq. (3) and Eq. (4) are the Maxwell equations, and Eq. (5) is Newton's equation for the p -th particle of species s .

C. Construction of the algorithm as a discrete field theory

According to the general principle of structure-preserving geometric algorithm, the first step is to discretize the field theory [1, 2, 4, 11, 12]. For the electromagnetic field, we use the technique of Whitney forms and discrete manifold [72, 74]. For example, in a tetrahedron mesh the magnetic field \mathbf{B} as a 2-form field can be discretized on a 2-simplex σ_2 (a side of

a 3D tetrahedron mesh) as $\int_{\sigma_2} \mathbf{B} \cdot d\mathbf{S}$, where \mathbf{S} is the unit normal vector of σ_2 . Note that σ_2 is a common side of two tetrahedron cells. In a mesh constructed using a curvilinear orthogonal coordinate system, which will be referred to as a Curvilinear Orthogonal Mesh (COM), such discretization can be also performed. Let

$$\phi_{i,j,k,l} = \phi(x_{J,l}^4) , \quad (6)$$

$$\mathbf{A}_{i,j,k,l} = \begin{bmatrix} A_{x_1}(x_{J,l}^4) h_1(x_{J,l}^4) , \\ A_{x_2}(x_{J,l}^4) h_2(x_{J,l}^4) , \\ A_{x_3}(x_{J,l}^4) h_3(x_{J,l}^4) \end{bmatrix}^T , \quad (7)$$

$$\mathbf{B}_{i,j,k,l} = \begin{bmatrix} B_{x_1}(x_{J,l}^4) h_2(x_{J,l}^4) h_3(x_{J,l}^4) , \\ B_{x_2}(x_{J,l}^4) h_3(x_{J,l}^4) h_1(x_{J,l}^4) , \\ B_{x_3}(x_{J,l}^4) h_1(x_{J,l}^4) h_2(x_{J,l}^4) \end{bmatrix}^T , \quad (8)$$

$$\rho_{i,j,k,l} = \rho(x_{J,l}^4) h_1(x_{J,l}^4) h_2(x_{J,l}^4) h_3(x_{J,l}^4) , \quad (9)$$

where $(x_{J,l}^4)$ denotes $(i\Delta x_1, j\Delta x_2, k\Delta x_3, l\Delta t)$, $\phi_{i,j,k,l}$, $\mathbf{A}_{i,j,k,l}$, $\mathbf{B}_{i,j,k,l}$ and $\rho_{i,j,k,l}$ are discrete 0-, 1-, 2- and 3-forms, respectively. In this discretization, the discrete gradient, curl and divergence operators can simply be finite difference operators. In the present study, the following difference operators are adopted,

$$(\nabla_d \phi)_{i,j,k} = [\phi_{i+1,j,k} - \phi_{i,j,k}, \phi_{i,j+1,k} - \phi_{i,j,k}, \phi_{i,j,k+1} - \phi_{i,j,k}] , \quad (10)$$

$$(\text{curl}_d \mathbf{A})_{i,j,k} = \begin{bmatrix} (A_{x_3 i,j+1,k} - A_{x_3 i,j,k}) - (A_{x_2 i,j,k+1} - A_{x_2 i,j,k}) \\ (A_{x_1 i,j,k+1} - A_{x_1 i,j,k}) - (A_{x_3 i+1,j,k} - A_{x_3 i,j,k}) \\ (A_{x_2 i+1,j,k} - A_{x_2 i,j,k}) - (A_{x_1 i,j+1,k} - A_{x_1 i,j,k}) \end{bmatrix}^T , \quad (11)$$

$$(\text{div}_d \mathbf{B})_{i,j,k} = (B_{x_1 i+1,j,k} - B_{x_1 i,j,k}) + (B_{x_2 i,j+1,k} - B_{x_2 i,j,k}) + (B_{z i,j,k+1} - B_{z i,j,k}) . \quad (12)$$

To discretize the particle-field interaction while preserving geometric structures and symmetries, Whitney interpolating forms [74] and their high-order generalizations [4] are used. Akin to previous results on Whitney interpolating forms in a cubic mesh [4], interpolating forms $W_{O\sigma_0 J}(\mathbf{x})$, $W_{O\sigma_1 J}(\mathbf{x})$, $W_{O\sigma_2 J}(\mathbf{x})$ and $W_{O\sigma_3 J}(\mathbf{x})$ for 0-, 1-, 2- and 3-forms can be

constructed on a COM as follows,

$$W_{O\sigma_0J}(\mathbf{x}) = W_{\sigma_0J}(\mathbf{x}) , \quad (13)$$

$$W_{O\sigma_1J}(\mathbf{x}) = W_{\sigma_1J}(\mathbf{x}) / [h_1(\mathbf{x}), h_2(\mathbf{x}), h_3(\mathbf{x})] , \quad (14)$$

$$W_{O\sigma_2J}(\mathbf{x}) = W_{\sigma_2J}(\mathbf{x}) / [h_2(\mathbf{x}) h_3(\mathbf{x}), h_3(\mathbf{x}) h_1(\mathbf{x}), h_1(\mathbf{x}) h_2(\mathbf{x})] , \quad (15)$$

$$W_{O\sigma_3J}(\mathbf{x}) = W_{\sigma_3J}(\mathbf{x}) / h_1(\mathbf{x}) h_2(\mathbf{x}) h_3(\mathbf{x}) , \quad (16)$$

where $W_{\sigma_iJ}(\mathbf{x}), 0 \leq i \leq 3$ are the interpolating forms in a cubic mesh defined in Ref. [4] and the quotient (product) of vectors means component-wise quotient (product), i.e.,

$$[A_{x_1}, A_{x_2}, A_{x_3}] / [B_{x_1}, B_{x_2}, B_{x_3}] = \left[\frac{A_{x_1}}{B_{x_1}}, \frac{A_{x_2}}{B_{x_2}}, \frac{A_{x_3}}{B_{x_3}} \right] . \quad (17)$$

With these operators and interpolating forms, we discretize the action integral as

$$\begin{aligned} \mathcal{A}_d = & \sum_{s,p,l} (L_{sp}(m_s, \mathbf{v}_{sp,l}) + q_s (\overline{\mathbf{v}_{sp} \cdot \mathbf{A}}(\mathbf{x}_{sp,l}, \mathbf{x}_{sp,l+1}, l) - \phi(\mathbf{x}_{sp,l+1}, l+1))) + \\ & \frac{h_{\sigma_3}(\mathbf{x}_J)}{2} \sum_J \left(\left(-\frac{\mathbf{A}_{J,l+1} - \mathbf{A}_{J,l}}{\Delta t \mathbf{h}_{\sigma_1}(\mathbf{x}_J)} - \frac{(\nabla_d \phi)_{J,l+1}}{\mathbf{h}_{\sigma_1}(\mathbf{x}_J)} \right)^2 - \left(\frac{(\text{curl}_d \mathbf{A})_{K,l}}{\mathbf{h}_{\sigma_2}(\mathbf{x}_K)} \right)^2 \right) , \quad (18) \end{aligned}$$

where l is the index for the temporal grid, J is the index vector for the spatial grid, and

$$\mathbf{h}_{\sigma_1}(\mathbf{x}) = [h_1(\mathbf{x}), h_2(\mathbf{x}), h_3(\mathbf{x})], \quad (19)$$

$$\mathbf{h}_{\sigma_2}(\mathbf{x}) = [h_2(\mathbf{x})h_3(\mathbf{x}), h_3(\mathbf{x})h_1(\mathbf{x}), h_1(\mathbf{x})h_2(\mathbf{x})], \quad (20)$$

$$h_{\sigma_3}(\mathbf{x}) = h_1(\mathbf{x})h_2(\mathbf{x})h_3(\mathbf{x}), \quad (21)$$

$$\mathbf{v}_{sp,l} = \frac{\mathbf{x}_{sp,l+1} - \mathbf{x}_{sp,l}}{\Delta t} \mathbf{h}_{\sigma_1} \left(\frac{\mathbf{x}_{sp,l+1} + \mathbf{x}_{sp,l}}{2} \right), \quad (22)$$

$$\phi(\mathbf{x}, l) = \sum_J \phi_{J,l} W_{\sigma_0 J}(\mathbf{x}), \quad (23)$$

$$\begin{aligned} \overline{\mathbf{v}_{sp} \cdot \mathbf{A}}(\mathbf{x}_{sp,l}, \mathbf{x}_{sp,l+1}, l) &= \int_0^1 d\tau \left[\begin{aligned} &\frac{x_{1,sp,l+1} - x_{1,sp,l}}{\Delta t} h_1(x_{1,sp,l} + \tau(x_{1,sp,l+1} - x_{1,sp,l}), x_{2,sp,l}, x_{3,sp,l}), \\ &\frac{x_{2,sp,l+1} - x_{2,sp,l}}{\Delta t} h_2(x_{1,sp,l+1}, x_{2,sp,l} + \tau(x_{2,sp,l+1} - x_{2,sp,l}), x_{3,sp,l}), \\ &\frac{x_{3,sp,l+1} - x_{3,sp,l}}{\Delta t} h_3(x_{1,sp,l+1}, x_{2,sp,l+1}, x_{3,sp,l} + \tau(x_{3,sp,l+1} - x_{3,sp,l})) \end{aligned} \right] \\ &\cdot \left[\begin{aligned} &\tilde{A}_{x_1,l}(x_{1,sp,l} + \tau(x_{1,sp,l+1} - x_{1,sp,l}), x_{2,sp,l}, x_{3,sp,l}), \\ &\tilde{A}_{x_2,l}(x_{1,sp,l+1}, x_{2,sp,l} + \tau(x_{2,sp,l+1} - x_{2,sp,l}), x_{3,sp,l}), \\ &\tilde{A}_{x_3,l}(x_{1,sp,l+1}, x_{2,sp,l+1}, x_{3,sp,l} + \tau(x_{3,sp,l+1} - x_{3,sp,l})) \end{aligned} \right] \quad (24) \end{aligned}$$

$$\begin{aligned} &= \int_0^1 d\tau \left[\frac{x_{1,sp,l+1} - x_{1,sp,l}}{\Delta t}, \frac{x_{2,sp,l+1} - x_{2,sp,l}}{\Delta t}, \frac{x_{3,sp,l+1} - x_{3,sp,l}}{\Delta t} \right] \\ &\cdot \left[\begin{aligned} &A_{x_1,l}(x_{1,sp,l} + \tau(x_{1,sp,l+1} - x_{1,sp,l}), x_{2,sp,l}, x_{3,sp,l}), \\ &A_{x_2,l}(x_{1,sp,l+1}, x_{2,sp,l} + \tau(x_{2,sp,l+1} - x_{2,sp,l}), x_{3,sp,l}), \\ &A_{x_3,l}(x_{1,sp,l+1}, x_{2,sp,l+1}, x_{3,sp,l} + \tau(x_{3,sp,l+1} - x_{3,sp,l})) \end{aligned} \right], \quad (25) \end{aligned}$$

$$\begin{bmatrix} \tilde{A}_{x_1,l}(\mathbf{x}), \\ \tilde{A}_{x_2,l}(\mathbf{x}), \\ \tilde{A}_{x_3,l}(\mathbf{x}) \end{bmatrix} \equiv \sum_J \mathbf{A}_{J,l} W_{O\sigma_1 J}(\mathbf{x}), \quad (26)$$

$$\begin{bmatrix} A_{x_1,l}(\mathbf{x}), \\ A_{x_2,l}(\mathbf{x}), \\ A_{x_3,l}(\mathbf{x}) \end{bmatrix} \equiv \sum_J \mathbf{A}_{J,l} W_{\sigma_1 J}(\mathbf{x}). \quad (27)$$

Finally, the time advance rule is given by the variation of the action integral with respect to the discrete fields,

$$\frac{\partial \mathcal{A}_d}{\partial \mathbf{x}_{sp,l}} = 0, \quad (28)$$

$$\frac{\partial \mathcal{A}_d}{\partial \mathbf{A}_{J,l}} = 0, \quad (29)$$

$$\frac{\partial \mathcal{A}_d}{\partial \phi_{J,l}} = 0. \quad (30)$$

From Eq. (28), the variation with respect to $\mathbf{x}_{sp,l}$ leads to

$$\frac{\partial}{\partial \mathbf{x}_l} (L_{sp}(m_s, \mathbf{v}_{sp,l-1}) + L_{sp}(m_s, \mathbf{v}_{sp,l})) = q_s (\mathbf{E}_l(\mathbf{x}_{sp,l}) + \overline{\mathbf{v}_{sp} \times \mathbf{B}}(l-1, l, l+1)) , \quad (31)$$

where

$$\mathbf{E}_l(\mathbf{x}) = \sum_J \mathbf{E}_{J,l} W_{\sigma_1 J}(\mathbf{x}) , \quad (32)$$

$$\mathbf{E}_{J,l} = -\frac{\mathbf{A}_{J,l} - \mathbf{A}_{J,l-1}}{\Delta t} , \quad (33)$$

$$\overline{\mathbf{v}_{sp} \times \mathbf{B}}(l-1, l, l+1) = \frac{1}{\Delta t} \left[\begin{array}{l} \int_{x_{2,sp,l-1}}^{x_{2,sp,l}} dx_2 B_{x_3,l-1}(x_{1,sp,l}, x_2, x_{3,sp,l-1}) , \\ \int_{x_{3,sp,l-1}}^{x_{3,sp,l}} dx_3 B_{x_1,l-1}(x_{1,sp,l}, x_{2,sp,l}, x_3) , \\ \int_{x_{1,sp,l}}^{x_{1,sp,l+1}} dx_1 B_{x_2,l}(x_1, x_{2,sp,l}, x_{3,sp,l}) \end{array} \right] \\ - \frac{1}{\Delta t} \left[\begin{array}{l} \int_{x_{3,sp,l-1}}^{x_{3,sp,l}} dx_3 B_{x_2,l-1}(x_{1,sp,l}, x_{2,sp,l}, x_3) , \\ \int_{x_{1,sp,l}}^{x_{1,sp,l+1}} dx_1 B_{x_3,l}(x_1, x_{2,sp,l}, x_{3,sp,l}) , \\ \int_{x_{2,sp,l}}^{x_{2,sp,l+1}} dx_2 B_{x_1,l}(x_{1,sp,l+1}, x_2, x_{3,sp,l}) \end{array} \right] , \quad (34)$$

$$\left[\begin{array}{l} B_{x_1,l}(\mathbf{x}) , \\ B_{x_2,l}(\mathbf{x}) , \\ B_{x_3,l}(\mathbf{x}) \end{array} \right] = \sum_J \mathbf{B}_{J,l} W_{\sigma_2 J}(\mathbf{x}) , \quad (35)$$

$$\mathbf{B}_{K,l} = \sum_J \text{curl}_{dK,J} \mathbf{A}_{J,l} . \quad (36)$$

To reduce simulation noise, we use 2nd-order Whitney forms for field interpolation. The concept of 2nd-order Whitney forms and their constructions were systematically developed in Ref. [4]. In general, only piece-wise polynomials are used to construct high-order Whitney forms, and it is straightforward to calculate integrals along particles' trajectories. These integrals can be calculated explicitly even with more complex Whitney interpolating forms, because these interpolating forms contain derivatives that are easy to integrate.

From Eq. (29), the discrete Ampere's law is

$$\frac{1}{\mathbf{h}_{\sigma_1}(\mathbf{x}_J) \mathbf{h}_{\sigma_1}(\mathbf{x}_J)} \frac{\mathbf{E}_{J,l+1} - \mathbf{E}_{J,l}}{\Delta t} h_{\sigma_3}(\mathbf{x}_J) = \sum_K \text{curl}_d^T{}_{J,K} \frac{h_{\sigma_3}(\mathbf{x}_J)}{\mathbf{h}_{\sigma_2}(\mathbf{x}_K) \mathbf{h}_{\sigma_2}(\mathbf{x}_K)} \mathbf{B}_{K,l} - \mathbf{j}_{J,l} ,$$

where

$$\mathbf{j}_{J,l} = \frac{1}{\Delta t} \sum_{s,p} q_s \int_{C_{sp,l,l+1}} W_{\sigma_1 J}(\mathbf{x}) d\mathbf{x} , \quad (37)$$

and the integral path $C_{sp,l,l+1}$ is defined as a zigzag path from $\mathbf{x}_{sp,l}$ to $\mathbf{x}_{sp,l+1}$, i.e.,

$$\begin{aligned} C_{sp,l,l+1} = & \{(x_{1,sp,l} + \tau(x_{1,sp,l+1} - x_{1,sp,l}), x_{2,sp,l}, x_{3,sp,l}) \mid \tau \in [0, 1)\} \cup \\ & \{(x_{1,sp,l+1}, x_{2,sp,l} + \tau(x_{2,sp,l+1} - x_{2,sp,l}), x_{3,sp,l}) \mid \tau \in [0, 1)\} \cup \\ & \{(x_{1,sp,l+1}, x_{2,sp,l+1}, x_{3,sp,l} + \tau(x_{3,sp,l+1} - x_{3,sp,l})) \mid \tau \in [0, 1)\} . \end{aligned} \quad (38)$$

Using the definition of $\mathbf{B}_{K,l}$, i.e., Eq. (36), we can obtain its discrete time evolution,

$$\frac{\mathbf{B}_{K,l} - \mathbf{B}_{K,l-1}}{\Delta t} = - \sum_J \text{curl}_{dK,J} \mathbf{E}_{J,l} , \quad (39)$$

which is the discrete version of Faraday's law.

Generally the above scheme is implicit. However, if particles are non-relativistic and the line element vector \mathbf{h} of a curvilinear orthogonal coordinate system satisfies the following condition,

$$\frac{\partial h_1}{\partial x_1} = \frac{\partial h_2}{\partial x_2} = \frac{\partial h_3}{\partial x_3} = 0 , \quad (40)$$

then high-order explicit schemes exist in the COM constructed using this coordinate system. The cylindrical coordinate is such a case. In Sec. II E we derive the 2nd-order explicit scheme for the non-relativistic Vlasov-Maxwell system in the cylindrical mesh.

D. Poisson bracket and its splitting algorithm in a curvilinear orthogonal mesh

For the structure-preserving geometric PIC algorithm presented in Sec. II C, there exists a corresponding discrete Poisson bracket. When particles are non-relativistic and condition (40) is satisfied, an associate splitting algorithm, which is explicit and symplectic, can be constructed. The algorithm is similar to and generalizes the explicit non-canonical symplectic splitting algorithm in the Cartesian coordinate system designed in Ref. [6]. Since the algorithm formulated in Sec. II C is independent from these constructions, we only list the results here without detailed derivations.

In a COM built on a curvilinear orthogonal coordinate system, we can choose to discretize the space only using the same method described above to obtain

$$\begin{aligned} L_{sd} = & \sum_{s,p} \left(L_{sp}(m_s, \dot{\mathbf{x}}_{sp}) + q_s \dot{\mathbf{x}}_{sp} \cdot \sum_J \mathbf{A}_J W_{\sigma_1 J}(\mathbf{x}_{sp}) \right) + \\ & \frac{1}{2} \sum_J \left(\left(\frac{-\dot{\mathbf{A}}_J}{\mathbf{h}_{\sigma_1}(\mathbf{x}_J)} \right)^2 - \left(\frac{(\text{curl}_{d\mathbf{A}})_{J,l}}{\mathbf{h}_{\sigma_2}(\mathbf{x}_J)} \right)^2 \right) h_{\sigma_3}(\mathbf{x}_J) , \end{aligned} \quad (41)$$

where the temporal gauge ($\phi = 0$) has been adopted. Following the procedure in Ref. [4], a non-canonical symplectic structure can be constructed from this Lagrangian, and the associated discrete Poisson bracket is

$$\begin{aligned}
\{F, G\} = & \sum_J \left(\frac{\partial F}{\partial \mathbf{E}_J} \cdot \frac{\text{diag}(\mathbf{h}_{\sigma 1}(\mathbf{x}_J)^2)}{h_{\sigma 3}(\mathbf{x}_J)} \cdot \sum_K \frac{\partial G}{\partial \mathbf{B}_K} \text{curl}_{dKJ} - \right. \\
& \left. \sum_K \frac{\partial F}{\partial \mathbf{B}_K} \text{curl}_{dKJ} \cdot \frac{\text{diag}(\mathbf{h}_{\sigma 1}(\mathbf{x}_J)^2)}{h_{\sigma 3}(\mathbf{x}_J)} \cdot \frac{\partial G}{\partial \mathbf{E}_J} \right) + \\
& \sum_{s,p} \frac{1}{m_s} \sum_{i=1}^3 \frac{1}{h_i(\mathbf{x}_{sp})^2} \left(\frac{\partial F}{\partial x_{i,sp}} \cdot \frac{\partial G}{\partial \dot{x}_{i,sp}} - \frac{\partial F}{\partial \dot{x}_{i,sp}} \cdot \frac{\partial G}{\partial x_{i,sp}} \right) + \sum_{s,p} \sum_J \sum_{i=1}^3 \\
& \frac{h_{\sigma 1, x_i}(\mathbf{x}_J)^2 q_s}{m_s h_i(\mathbf{x}_{sp})^2 h_{\sigma 3, x_i}(\mathbf{x}_J)} \left(\frac{\partial F}{\partial \dot{x}_{i,sp}} W_{\sigma 1 J}(x_{i,sp}) \frac{\partial G}{\partial E_{x_i, J}} - \frac{\partial G}{\partial \dot{x}_{i,sp}} W_{\sigma 1 J}(x_{i,sp}) \frac{\partial F}{\partial E_{x_i, J}} \right) \\
& + \sum_s \sum_K \frac{1}{m_s^2} \left(\text{diag} \left(\frac{1}{\mathbf{h}_{\sigma 1}(\mathbf{x}_{sp})^2} \right) \cdot \frac{\partial F}{\partial \dot{\mathbf{x}}_{sp}} \right) \cdot \\
& \left((\nabla_{\mathbf{x}_{sp}} \times (m_s \text{diag}(\mathbf{h}_{\sigma 1}(\mathbf{x}_{sp})^2) \cdot \dot{\mathbf{x}}_{sp}) + q_s W_{\sigma 2 K}(\mathbf{x}_{sp}) \mathbf{B}_K) \right. \\
& \left. \times \left(\frac{\partial G}{\partial \dot{\mathbf{x}}_{sp}} \cdot \text{diag} \left(\frac{1}{\mathbf{h}_{\sigma 1}(\mathbf{x}_{sp})^2} \right) \right) \right), \tag{42}
\end{aligned}$$

and the corresponding Hamiltonian is

$$H_{sd} = \frac{1}{2} \sum_J \left(\left| \frac{\mathbf{E}_J}{\mathbf{h}_{\sigma 1}(\mathbf{x}_J)} \right|^2 + \left| \frac{\mathbf{B}_{J,l}}{\mathbf{h}_{\sigma 2}(\mathbf{x}_J)} \right|^2 \right) h_{\sigma 3}(\mathbf{x}_J) + \sum_{sp} \sum_i \frac{m_s}{2} \dot{x}_{i,sp}^2 h_i(\mathbf{x}_{sp})^2. \tag{43}$$

Here particles are assumed to be non-relativistic and $\mathbf{E}_J, \mathbf{B}_K$ are spatially discretized electromagnetic fields defined as

$$\mathbf{E}_J = -\dot{\mathbf{A}}_J, \tag{44}$$

$$\mathbf{B}_K = \sum_J \text{curl}_{dKJ} \mathbf{A}_J. \tag{45}$$

The Poisson bracket given by Eq. (42) generalizes the previous Cartesian version [4] to arbitrary curvilinear orthogonal meshes. It automatically satisfies the Jacobi identity because it is derived from a Lagrangian 1-form. See Ref. [4] for detailed geometric constructions.

The dynamics equation, i.e., the Hamiltonian equation, is

$$\dot{F} = \{F, H_{sd}\}, \tag{46}$$

where

$$F = [\mathbf{E}_J, \mathbf{B}_J, \mathbf{x}_{sp}, \dot{\mathbf{x}}_{sp}] . \quad (47)$$

To build an explicit symplectic algorithm, we adopt the splitting method [6]. The Hamiltonian H_{sd} is divided into 5 parts,

$$H_{sd} = H_E + H_B + H_1 + H_2 + H_3 , \quad (48)$$

$$H_E = \frac{1}{2} \sum_J \left| \frac{\mathbf{E}_J}{\mathbf{h}_{\sigma 1}(\mathbf{x}_J)} \right|^2 h_{\sigma 3}(\mathbf{x}_J) , \quad (49)$$

$$H_B = \frac{1}{2} \sum_J \left| \frac{\mathbf{B}_{J,l}}{\mathbf{h}_{\sigma 2}(\mathbf{x}_J)} \right|^2 h_{\sigma 3}(\mathbf{x}_J) , \quad (50)$$

$$H_i = \sum_{sp} \frac{m_s}{2} \dot{x}_{i,sp}^2 h_i(\mathbf{x}_{sp})^2 \quad \text{for } i \text{ in } \{1, 2, 3\} . \quad (51)$$

Each part defines a sub-system with the same Poisson bracket (42). It turns out that when condition (40) is satisfied the exact solution of each subsystem can be written down in a closed form, and explicit high-order symplectic algorithms for the entire system can be constructed by compositions using the exact solutions of the sub-systems. For H_E and H_B , the corresponding Hamiltonian equations are

$$\dot{F} = \{F, H_E\} , \quad (52)$$

$$\dot{F} = \{F, H_B\} , \quad (53)$$

i.e.,

$$\begin{cases} \dot{\mathbf{E}}_J = 0 , \\ \dot{\mathbf{B}}_K = -\sum_J \text{curl}_{dKJ} \mathbf{E}_J , \\ \dot{\mathbf{x}}_{sp} = 0 , \\ \ddot{\mathbf{x}}_{sp} = \frac{q_s}{m_s} \text{diag} \left(\frac{1}{\mathbf{h}_{\sigma 1}(\mathbf{x}_{sp})^2} \right) \cdot \sum_J W_{\sigma 1J}(\mathbf{x}_{sp}) \mathbf{E}_J , \end{cases} \quad (54)$$

and

$$\begin{cases} \dot{\mathbf{E}}_J = \frac{\text{diag}(\mathbf{h}_{\sigma 1}(\mathbf{x}_J)^2)}{h_{\sigma 3}(\mathbf{x}_J)} \cdot \sum_K h_{\sigma 3}(\mathbf{x}_K) \text{diag} \left(\frac{1}{\mathbf{h}_{\sigma 2}(\mathbf{x}_K)^2} \right) \cdot \text{curl}_{dKJ} \mathbf{B}_K , \\ \dot{\mathbf{B}}_K = 0 , \\ \dot{\mathbf{x}}_{sp} = 0 , \\ \ddot{\mathbf{x}}_{sp} = 0 . \end{cases} \quad (55)$$

Their analytical solutions are

$$\Theta_E : \begin{cases} \mathbf{E}_J(t + \Delta t) = \mathbf{E}_J(t) , \\ \mathbf{B}_K(t + \Delta t) = \mathbf{B}_K(t) - \Delta t \sum_J \text{curl}_{dKJ} \mathbf{E}_J(t) , \\ \mathbf{x}_{sp}(t + \Delta t) = \mathbf{x}_s(t) , \\ \dot{\mathbf{x}}_{sp}(t + \Delta t) = \dot{\mathbf{x}}_s(t) + \Delta t \frac{q_s}{m_s} \text{diag} \left(\frac{1}{\mathbf{h}_{\sigma_1}(\mathbf{x}_{sp})^2} \right) \cdot \sum_J W_{\sigma_{1J}}(\mathbf{x}_{sp}(t)) \mathbf{E}_J(t) , \end{cases} \quad (56)$$

$$\Theta_B : \begin{cases} \mathbf{E}_J(t + \Delta t) = \mathbf{E}_J(t) + \Delta t \frac{\text{diag}(\mathbf{h}_{\sigma_1}(\mathbf{x}_J)^2)}{h_{\sigma_3}(\mathbf{x}_J)} \cdot \sum_K \text{curl}_{dKJ} h_{\sigma_3}(\mathbf{x}_K) \text{diag} \left(\frac{1}{\mathbf{h}_{\sigma_2}(\mathbf{x}_K)^2} \right) \cdot \mathbf{B}_K(t) , \\ \mathbf{B}_K(t + \Delta t) = \mathbf{B}_K(t) , \\ \mathbf{x}_{sp}(t + \Delta t) = \mathbf{x}_{sp}(t) , \\ \dot{\mathbf{x}}_{sp}(t + \Delta t) = \dot{\mathbf{x}}_{sp}(t) . \end{cases} \quad (57)$$

For H_1 , the dynamic equation is $\dot{F} = \{F, H_1\}$, or more specifically,

$$\begin{cases} \dot{\mathbf{E}}_J = - \sum_{sp} \frac{q_s}{h_{\sigma_3}(\mathbf{x}_J)} \text{diag}(\mathbf{h}_{\sigma_1}(\mathbf{x}_J)^2) \cdot \dot{x}_{1,sp} \mathbf{e}_1 W_{\sigma_{1J}}(\mathbf{x}_{sp}) , \\ \dot{\mathbf{B}}_K = 0 , \\ \dot{\mathbf{x}}_{sp} = \dot{x}_{1,sp} \mathbf{e}_1 , \\ \ddot{\mathbf{x}}_{sp} = - \text{diag} \left(\frac{1}{2\mathbf{h}_{\sigma_1}(\mathbf{x}_{sp})^2} \right) \cdot \nabla_{\mathbf{x}_{sp}} h_1(\mathbf{x}_{sp})^2 \dot{x}_{1,sp}^2 + \\ \text{diag} \left(\frac{1}{\mathbf{h}_{\sigma_1}(\mathbf{x}_{sp})^2} \right) \dot{x}_{1,sp} \mathbf{e}_1 \times (\nabla_{\mathbf{x}_{sp}} \times (\text{diag}(\mathbf{h}_{\sigma_1}(\mathbf{x}_{sp})^2 \cdot \dot{\mathbf{x}}_{sp}))) + \\ \text{diag} \left(\frac{q_s}{\mathbf{h}_{\sigma_1}(\mathbf{x}_{sp})^2 m_s} \right) \dot{x}_{1,sp} \mathbf{e}_1 \times \sum_K W_{\sigma_{2K}}(\mathbf{x}_s) \mathbf{B}_K . \end{cases} \quad (58)$$

Because the equation for $x_{1,sp}$ contains both $\dot{x}_{1,sp}$ and $\ddot{x}_{1,sp}$ explicitly, Eq. (58) is difficult to solve in general. However, when $\partial h_1(\mathbf{x}) / \partial x_1 = 0$, i.e.,

$$h_1(\mathbf{x}) = h_1(x_2, x_3) , \quad (59)$$

the dynamics equation for particles in Eq. (58) reduces to

$$\begin{cases} \dot{x}_{1,sp} = \dot{x}_{1,sp} , \\ \dot{x}_{2,sp} = 0 , \\ \dot{x}_{3,sp} = 0 , \\ \ddot{x}_{1,sp} h_1(\mathbf{x}_{sp})^2 = 0 , \\ \frac{d}{dt} (\dot{x}_{2,sp} h_2(\mathbf{x}_{sp})^2) = 2\dot{x}_{1,sp}^2 h_1(\mathbf{x}_{sp}) \frac{\partial h_1(\mathbf{x}_{sp})}{\partial x_{2,sp}} - \frac{q_s}{m_s} \dot{x}_{1,sp} \sum_K W_{\sigma_{2K}, x_3}(\mathbf{x}_{sp}) B_{x_3, K} \\ = \tilde{F}_{x_2}(\mathbf{x}_{sp}, \dot{x}_{1,sp}) , \\ \frac{d}{dt} (\dot{x}_{3,sp} h_3(\mathbf{x}_{sp})^2) = 2\dot{x}_{1,sp}^2 h_1(\mathbf{x}_{sp}) \frac{\partial h_1(\mathbf{x}_{sp})}{\partial x_{3,sp}} + \frac{q_s}{m_s} \dot{x}_{1,sp} \sum_K W_{\sigma_{2K}, x_2}(\mathbf{x}_{sp}) B_{x_2, K} \\ = \tilde{F}_{x_3}(\mathbf{x}_{sp}, \dot{x}_{1,sp}) . \end{cases} \quad (60)$$

In this case, Eq. (58) admits an analytical solution,

$$\Theta_1(\Delta t) : \left\{ \begin{array}{l} \mathbf{E}_J(t + \Delta t) = - \sum_{sp} \frac{q_s}{h_{\sigma 3}(\mathbf{x}_J)} \text{diag}(\mathbf{h}_{\sigma 1}(\mathbf{x}_J)^2) \cdot \int_0^{\Delta t} dt' \dot{x}_{1,sp} \mathbf{e}_1 W_{\sigma 1 J}(\mathbf{x}_{sp} + \mathbf{e}_1 \dot{x}_{1,sp} t') , \\ \mathbf{B}_K(t + \Delta t) = \mathbf{B}_K(t) , \\ x_{1,sp}(t + \Delta t) = x_{1,sp}(t) + \dot{x}_{1,sp}(t) \Delta t , \\ x_{2,sp}(t + \Delta t) = x_{2,sp}(t) , \\ x_{3,sp}(t + \Delta t) = x_{3,sp}(t) , \\ \dot{x}_{1,sp}(t + \Delta t) = \dot{x}_{1,sp}(t) , \\ \dot{x}_{2,sp}(t + \Delta t) = \frac{h_2(\mathbf{x}_{sp}(t))^2}{h_2(\mathbf{x}_{sp}(t) + \mathbf{e}_1 \dot{x}_{1,sp} \Delta t)^2} \dot{x}_{2,sp}(t) + \\ \frac{1}{h_2(\mathbf{x}_{sp}(t) + \mathbf{e}_1 \dot{x}_{1,sp} \Delta t)^2} \int_0^{\Delta t} dt' \tilde{F}_{x_2}(\mathbf{x}_{sp} + \mathbf{e}_1 \dot{x}_{1,sp} t', \dot{x}_{1,sp}) , \\ \dot{x}_{3,sp}(t + \Delta t) = \frac{h_3(\mathbf{x}_{sp}(t))^2}{h_3(\mathbf{x}_{sp}(t) + \mathbf{e}_1 \dot{x}_{1,sp} \Delta t)^2} \dot{x}_{3,sp}(t) + \\ \frac{1}{h_3(\mathbf{x}_{sp}(t) + \mathbf{e}_1 \dot{x}_{1,sp} \Delta t)^2} \int_0^{\Delta t} dt' \tilde{F}_{x_3}(\mathbf{x}_{sp} + \mathbf{e}_1 \dot{x}_{1,sp} t', \dot{x}_{1,sp}) . \end{array} \right. \quad (61)$$

Similarly, analytical solutions Θ_2 (Θ_3) for H_2 (H_3) can be also derived when $\partial h_2(\mathbf{x})/\partial x_2 = \partial h_3(\mathbf{x})/\partial x_3 = 0$. Finally, we can compose these analytical solutions to obtain explicit symplectic integration algorithms for the entire system. For example, a first order scheme can be constructed as

$$\Theta_1(\Delta t) = \Theta_E(\Delta t) \Theta_B(\Delta t) \Theta_x(\Delta t) \Theta_y(\Delta t) \Theta_z(\Delta t) , \quad (62)$$

and a second order symmetric scheme is

$$\begin{aligned} \Theta_2(\Delta t) &= \Theta_x(\Delta t/2) \Theta_y(\Delta t/2) \Theta_z(\Delta t/2) \Theta_B(\Delta t/2) \Theta_E(\Delta t) \\ &\quad \Theta_B(\Delta t/2) \Theta_z(\Delta t/2) \Theta_y(\Delta t/2) \Theta_x(\Delta t/2) . \end{aligned} \quad (63)$$

An algorithm with order $2(l+1)$ can be constructed in the following way,

$$\Theta_{2(l+1)}(\Delta t) = \Theta_{2l}(\alpha_l \Delta t) \Theta_{2l}(\beta_l \Delta t) \Theta_{2l}(\alpha_l \Delta t) , \quad (64)$$

$$\alpha_l = 1/(2 - 2^{1/(2l+1)}) , \quad (65)$$

$$\beta_l = 1 - 2\alpha_l . \quad (66)$$

E. High-order explicit structure-preserving geometric PIC algorithm in a cylindrical mesh

Magnetic fusion plasmas are often confined in the toroidal geometry, for which the cylindrical coordinate system is convenient. We now present the high-order explicit structure-preserving geometric PIC algorithm in a cylindrical mesh. In this coordinate system, the

line element is

$$ds^2 = (dr)^2 + \left(\frac{r + R_0}{R_0} d(R_0\xi) \right)^2 + (dz)^2 , \quad (67)$$

where R_0 is a fixed radial length, $r + R_0$ is the radius in the standard cylindrical coordinate system, and $R_0\xi$ is the polar angle coordinate normalized by $1/R_0$. For typical applications in tokamak physics, R_0 is the major radius and ξ is called toroidal angle. To simplify the notation, we also refer to $(r, R_0\xi, z)$ as (x, y, z) .

For non-relativistic particles in the cylindrical mesh, if the discrete velocity in Eq. (22) is changed to

$$\mathbf{v}_{sp,l} = \frac{\mathbf{x}_{sp,l+1} - \mathbf{x}_{sp,l}}{\Delta t} \mathbf{h}_{\sigma 1}(\mathbf{x}_{sp,l+1}) , \quad (68)$$

then the 1st-order scheme given by Eq. (28) will be explicit. To construct an explicit 2nd-order scheme, the 2nd-order action integral can be chosen as

$$\begin{aligned} \mathcal{A}_{d2} = & \sum_{s,p,l} \frac{1}{2} \left(L_{sp}(m_s, \mathbf{v}_{sp,2l}) + L_{sp}(m_s, \mathbf{v}_{sp,2l+1}^*) + \right. \\ & q_s \left(2\overline{\mathbf{v}_{sp} \cdot \mathbf{A}}(\mathbf{x}_{sp,2l}, \mathbf{x}_{sp,2l+1}, l) + 2\overline{\mathbf{v}_{sp}^* \cdot \mathbf{A}}(\mathbf{x}_{sp,2l+1}, \mathbf{x}_{sp,2l+2}, l) - 2\phi(\mathbf{x}_{sp,2l+2}, l+1) \right) \\ & \left. + \frac{1}{2} \sum_J \left(\left(\left(-\frac{\mathbf{A}_{J,l+1} - \mathbf{A}_{J,l}}{\Delta t} - (\nabla_d \phi)_{J,l+1} \right) \frac{1}{\mathbf{h}_{\sigma 1}(\mathbf{x}_J)} \right)^2 - \left(\frac{(\text{curl}_d \mathbf{A})_{K,l}}{\mathbf{h}_{\sigma 2}(\mathbf{x}_K)} \right)^2 \right) h_{\sigma 3}(\mathbf{x}_J) \right) \quad (69) \end{aligned}$$

where

$$\begin{aligned} \mathbf{v}_{sp,2l} &= 2 \frac{\mathbf{x}_{2l+1} - \mathbf{x}_{2l}}{\Delta t} \mathbf{h}_{\sigma 1}(\mathbf{x}_{sp,2l+1}) , \\ \mathbf{v}_{sp,2l+1}^* &= 2 \frac{\mathbf{x}_{2l+2} - \mathbf{x}_{2l+1}}{\Delta t} \mathbf{h}_{\sigma 1}(\mathbf{x}_{sp,2l+1}) , \\ \overline{\mathbf{v}_{sp}^* \cdot \mathbf{A}}(\mathbf{x}_{sp,2l+1}, \mathbf{x}_{sp,2l+2}, l) &= \int_0^1 d\tau \\ & \left[\frac{x_{1,sp,2l+2} - x_{1,sp,2l+1}}{\Delta t}, \frac{x_{2,sp,2l+2} - x_{2,sp,2l+1}}{\Delta t}, \frac{x_{3,sp,2l+2} - x_{3,sp,2l+1}}{\Delta t} \right] \\ & \cdot \left[\begin{array}{l} A_{x_1,l}(x_{1,sp,2l+1} + \tau(x_{1,sp,2l+2} - x_{1,sp,2l+1}), x_{2,sp,2l+2}, x_{3,sp,2l+2}), \\ A_{x_2,l}(x_{1,sp,2l+1}, x_{2,sp,2l+1} + \tau(x_{2,sp,2l+2} - x_{2,sp,2l+1}), x_{3,sp,2l+2}), \\ A_{x_3,l}(x_{1,sp,2l+1}, x_{2,sp,2l+1}, x_{3,sp,2l+1} + \tau(x_{3,sp,2l+2} - x_{3,sp,2l+1})) \end{array} \right] . \end{aligned}$$

Taking the following discrete variation yields discrete time-advance rules,

$$\frac{\partial \mathcal{A}_{d2}}{\partial \mathbf{x}_{2l}} = 0 , \quad (70)$$

$$\frac{\partial \mathcal{A}_{d2}}{\partial \mathbf{x}_{2l+1}} = 0 , \quad (71)$$

$$\frac{\partial \mathcal{A}_{d2}}{\partial \mathbf{A}_{J,l}} = 0 , \quad (72)$$

$$\frac{\partial \mathcal{A}_{d2}}{\partial \phi_{J,l}} = 0 . \quad (73)$$

The explicit expressions for these time-advance are listed in Appendix B. Higher-order discrete action integral for building explicit schemes can be also derived using a similar technique, or using the splitting method described in Sec. IID.

In addition, we have also implemented the 1st-order relativistic charge-conserving geometric PIC in the cylindrical mesh. However the particle pusher in the relativistic scheme is implicit, and it is about 4 times slower than the explicit scheme. When studying relativistic effects, the implicit relativistic algorithm can be applied without significantly increasing the computational cost.

III. WHOLE-DEVICE 6D KINETIC SIMULATIONS OF TOKAMAK PHYSICS

The high-order explicit structure-preserving geometric PIC algorithm in a cylindrical mesh described in Sec. IIE has been implemented in the *SymPIC* code, designed for high-efficiency massively-parallel PIC simulations in modern clusters. The *OpenMP-MPI* version of *SymPIC* is available at <https://github.com/JianyuanXiao/SymPIC/>. The algorithm and code have been used to carry out the first-ever whole-device 6D kinetic simulations of tokamak physics. In this section, we report simulation results using machine parameters similar to those of the Alcator C-Mod tokamak [57, 58]. Two physics problems are studied, the self-consistent kinetic steady state and kinetic ballooning mode instabilities in the self-consistent kinetic steady state.

A. Axisymmetric self-consistent kinetic steady state in a tokamak

Kinetic equilibrium is the starting point for analytical and numerical studies of kinetic instabilities and associated transport phenomena. Because no self-consistent kinetic equilib-

Major radius R_0	Minor radius a	Plasma current I_p	Edge safe factor q_{95}	Toroidal magnetic field at R_0 (B_0)
0.69m	0.21m	0.54MA	About 3.5	4.2T

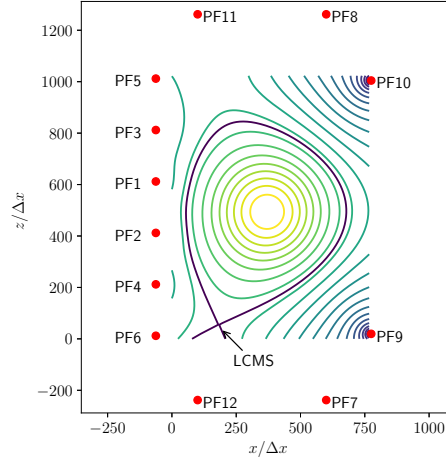
Table I: Machine parameters of the simulated tokamak. This set of parameters is similar to those of the Alcator C-Mod tokamak.

rium is known in the tokamak geometry, most previous studies adopted non-self-consistent distributions as assumed kinetic equilibria, especially for simulations based on the δf -method. Here, we numerically obtain an axisymmetric self-consistent kinetic steady state for a small tokamak using parameters similar to those of the Alcator C-Mod tokamak [57, 58]. The machine parameters are tabulated in Table I. The device is numerically constructed with Poloidal Field (PF) coils displayed in Fig. 1(a).

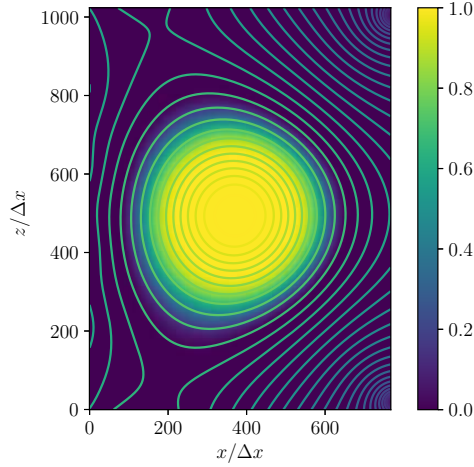
At the beginning of the simulation, non-equilibrium distributions for deuterium ions and electrons are loaded into the device. The initial density profile in the poloidal plane is shown in Fig. 1(b). The 2D profiles of the external field and initial velocity and temperature profiles for both species are plotted in Fig. 2. Simulation parameters are chosen as

$$\begin{aligned}
\Delta x &= 8 \times 10^{-4} \text{m}, \quad \Delta t = 0.1 \Delta x / c, \quad R_0 = 500 \Delta x, \\
T_{e,0} &= T_{i,0} = T_0 = 800 \text{eV}, \quad n_{e,0} = n_{i,0} = 5.0 \times 10^{19} \text{m}^{-3}, \\
m_i &= 3672 m_e = 3.34 \times 10^{-27} \text{kg}, \\
J_{PF,i} &= 67.9 \text{kA}, \quad \text{for } 1 \leq i \leq 6, \\
J_{PF,7} &= J_{PF,8} = 211.1 \text{kA}, \quad J_{PF,9} = J_{PF,10} = 238.1 \text{kA}, \\
J_{PF,11} &= -189.9 \text{kA}, \quad J_{PF,12} = -211.1 \text{kA}.
\end{aligned}$$

Detailed calculation of the external magnetic field, initial particle distributions, and boundary setup are outlined in Appendix A. Simulations show that the system reaches a steady state after 1.6×10^7 time-steps. At this time, the amplitude of magnetic perturbation at the middle plane of the edge ($x = 0.48 \text{m}$ and $z = 0.41 \text{m}$) is smaller than $B_0/200$, and the oscillation of position of plasma core is very small. Therefore, we can treat this state as a steady state. One such calculation requires about 1.3×10^5 core-hours on the Tianhe 3 prototype cluster. Profiles of flow velocities, densities, temperatures of electrons and ions as well as electromagnetic field at the steady state are shown in Figs. 3-6.



(a) Locations of PF coils and poloidal field lines.



(b) Initial plasma density profile ($5 \times 10^{19} \text{m}^{-3}$).

Figure 1: Poloidal field and initial plasma density profile.

From Fig. 3, the flow velocity of ions at the steady state is in the range of 10km/s, which is consistent with experimental observations [13, 14] and theoretical calculations [15, 16]. This ion flow is much slower than the thermal velocity of ions and thus is negligible in the force balance for the steady state, which can be written as

$$\mathbf{j} \times \mathbf{B} - \nabla \cdot \mathbf{p} = 0 . \quad (74)$$

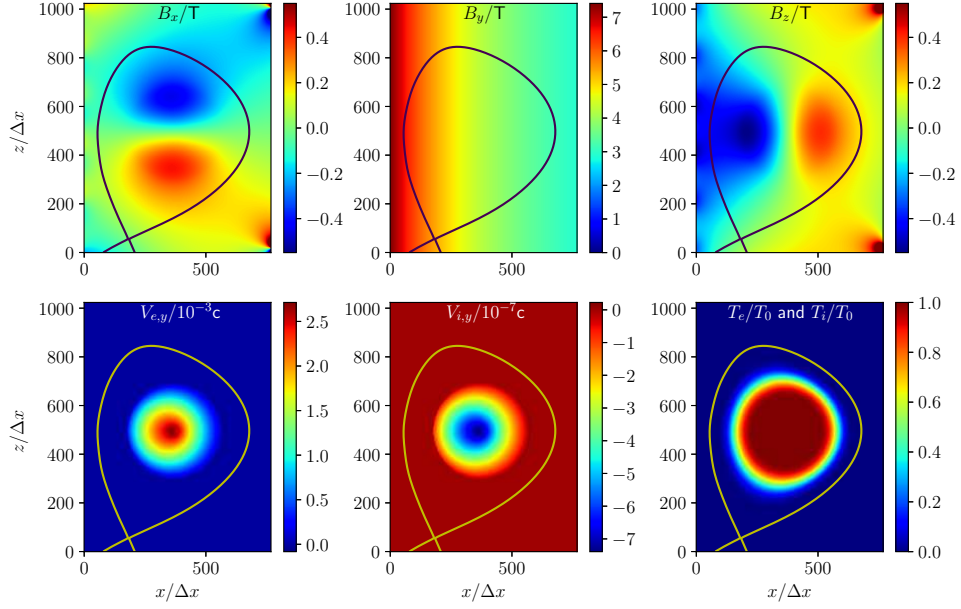


Figure 2: Tokamak external magnetic field and initial profiles of flow velocities in the \mathbf{e}_y direction and temperatures.

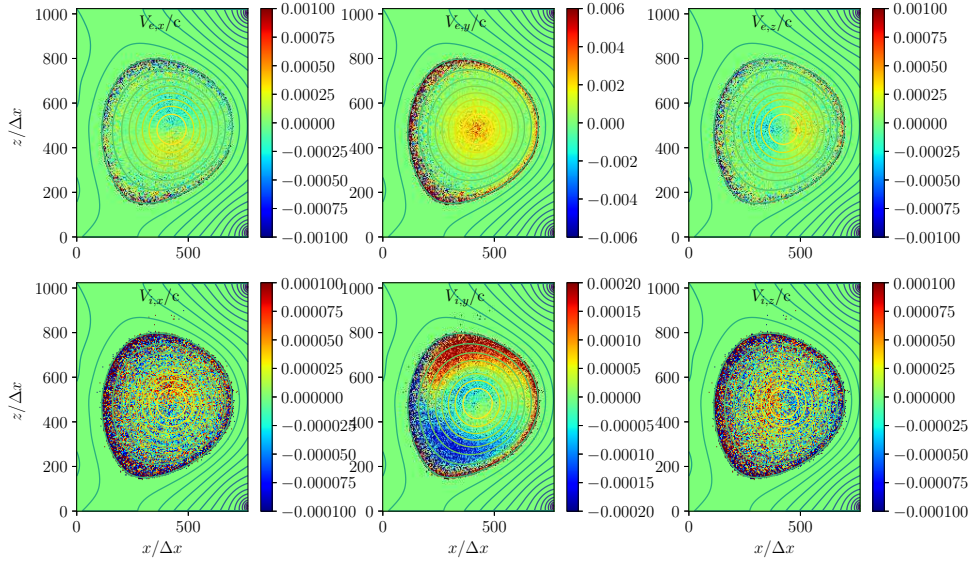


Figure 3: Flow velocity distributions for electrons and ions at the steady state.

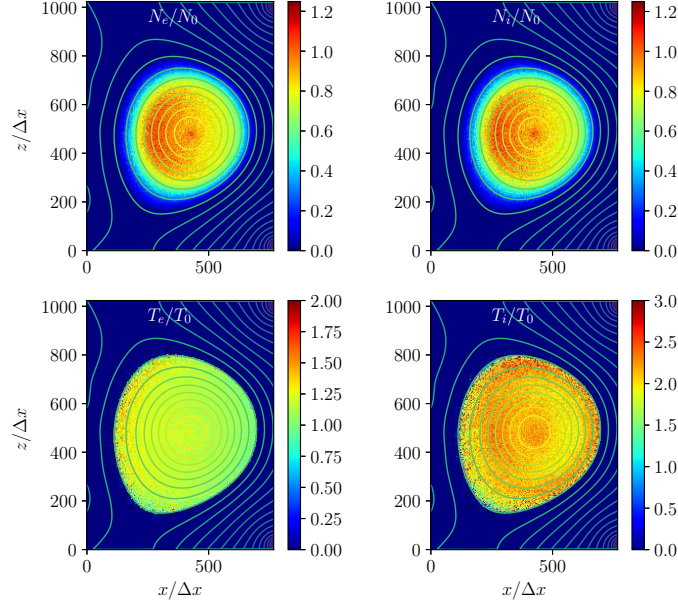


Figure 4: Density and temperature profiles of electrons and ions at the steady state.

Here, \mathbf{p} is the pressure tensor. Equation (74) is obtained by the familiar procedure of taking the second moment of the Vlasov equation, subtracting the flow velocity and summing over species. From the simulation data, the p_{ij} component of the pressure tensor is calculated as

$$p_{ij,J} = \sum_{\mathbf{x}_{sp} \in \text{grid } J} m_s v'_{i,sp} v'_{j,sp}, \quad \text{for } i, j \text{ in } \{x, y, z\}, \quad (75)$$

$$\mathbf{v}'_{sp} \equiv \mathbf{v}_{sp} - \left(\sum_{\mathbf{x}_{sp} \in \text{grid } J} \mathbf{v}_{sp} \right) / \left(\sum_{\mathbf{x}_{sp} \in \text{grid } J} 1 \right). \quad (76)$$

The profile of pressure tensor at the steady state at $z = 0.41\text{m}$ is shown in Fig. 7. Clearly, the pressure tensor is predominately diagonal and anisotropic with $p_{yy} > p_{xx} \approx p_{zz}$. Note that the pressure is almost isotropic in the poloidal plane, which indicates that it is valid to adopt the ideal magnetohydrodynamics (MHD) model with a scalar pressure for force balance in the 2D tokamak equilibrium. However, for 3D physics, the effect of pressure anisotropy needs to be considered. Since the steady state is 2D in space for the present case,

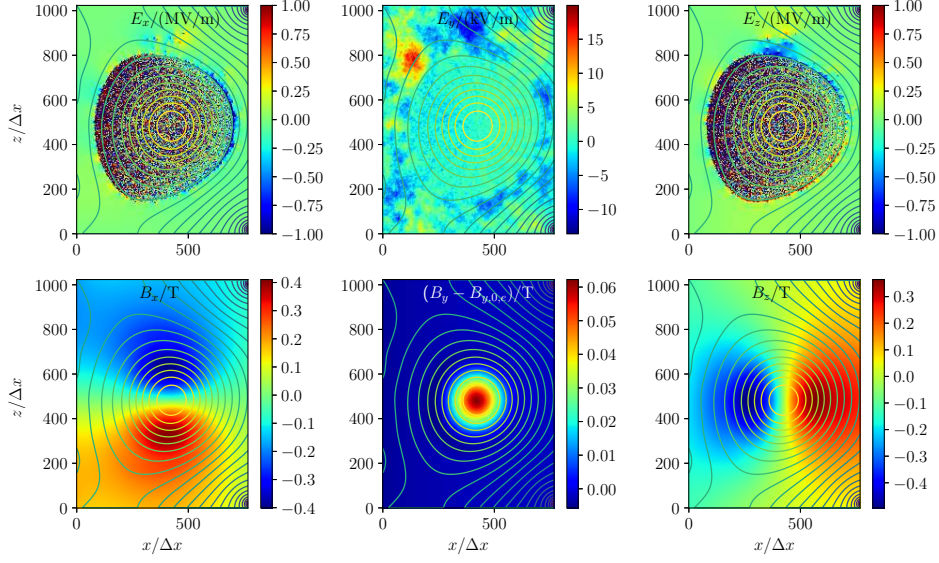


Figure 5: Electromagnetic field profiles at the steady state.

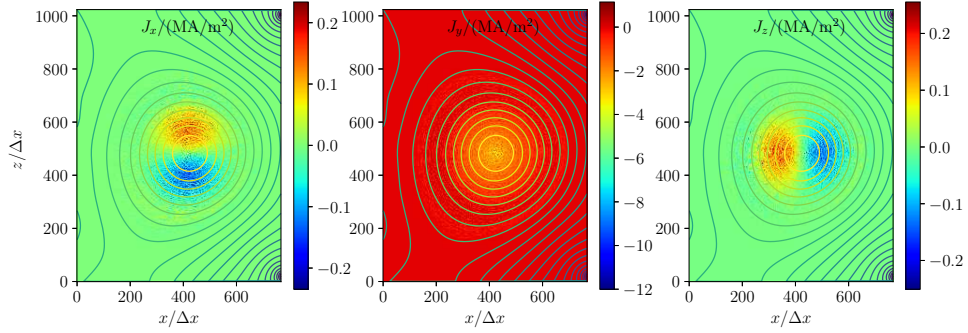


Figure 6: Current profiles at the steady state.

the force balance equation reduces to

$$\frac{\partial p_{xx}}{\partial x} = (\mathbf{j} \times \mathbf{B})_x, \quad (77)$$

$$\frac{\partial p_{zz}}{\partial z} = (\mathbf{j} \times \mathbf{B})_z. \quad (78)$$

To verify the force balance of the steady state, the four terms in Eqs. (77) and (78) are plotted in Fig. 8. For comparison, the components of $\partial p_{yy}/\partial x$ and $\partial p_{yy}/\partial z$ are also plotted. Figure 8 shows that the force balance is approximately satisfied for the numerically obtained steady state, which can be viewed as a self-consistent kinetic steady state.

To verify the energy conservation in the simulation, we have recorded the time-history of

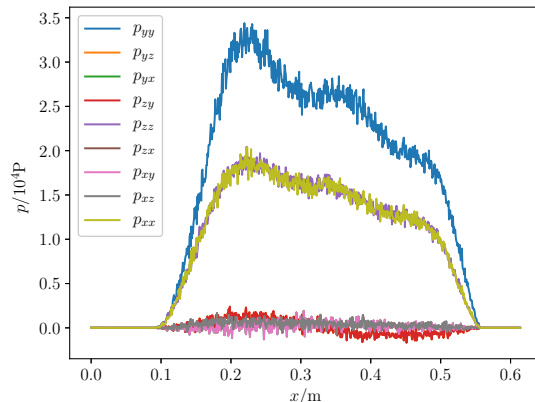


Figure 7: Pressure tensor profile at $z = 0.41\text{m}$.

the total energy in Fig. 9. The total energy drops a little, because some particles outside the last closed magnetic surface hit the simulation boundary, and these particles are removed from the simulation.

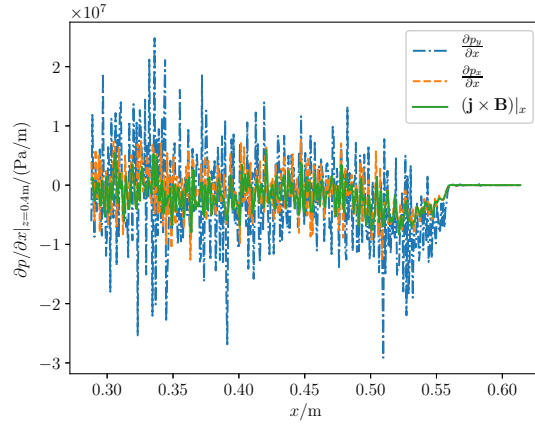
Before reaching the kinetic steady state, the plasma oscillates in the poloidal plane. It is expected that this oscillation can be described as an MHD process whose characteristic velocity is the Alfvén velocity $v_A = B_0/\sqrt{\mu_0 n_i m_i}$. To observe this oscillation, we plot in Fig. 10 the evolution of the magnetic field at $x = 600\Delta x$ and $z = 512\Delta x$. From the parameters of the simulation, the characteristic frequency of the oscillation is

$$\omega_A = \frac{v_A}{qR_0} \sim 2.26 \times 10^{-2} \omega_{c,i} , \quad (79)$$

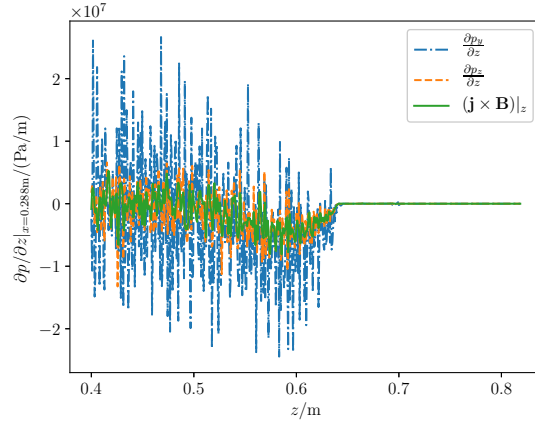
which agrees with the frequency of the B_x oscillation in Fig. 10.

B. Kinetic ballooning mode in tokamak

Kinetic Ballooning Mode (KBM) [120], characterized by both electromagnetic perturbations of the MHD type and nontrivial kinetic effects, plays an important role in tokamak edge physics. Traditionally, it has been simulated using electromagnetic gyrokinetic codes such as the Kin-2DEM [17, 18], LIGKA [121], GTC [19, 45] and GEM [50]. However, for edge plasmas, the gyrokinetic ordering [122–134] may become invalid under certain parameter regimes for modern tokamaks. For instance, the characteristic length in the edge of the H-mode plasma simulated by Wan et al. [135, 136] can be as short as about 5 times of the gyroradius of thermal ions, and in this situation, the gyrokinetic density calculation may be



(a) \mathbf{e}_x direction



(b) \mathbf{e}_z direction

Figure 8: Pressure gradient $\nabla \cdot \mathbf{p}$ and Lorentz force $\mathbf{j} \times \mathbf{B}$ in the \mathbf{e}_x (a) and \mathbf{e}_z (b) directions.

inaccurate. We have applied *SymPIC* code developed to carry out the first whole-device 6D kinetic simulations of the KBM in a tokamak geometry.

The machine parameters are the same as in Sec. III A. To trigger the KBM instability,

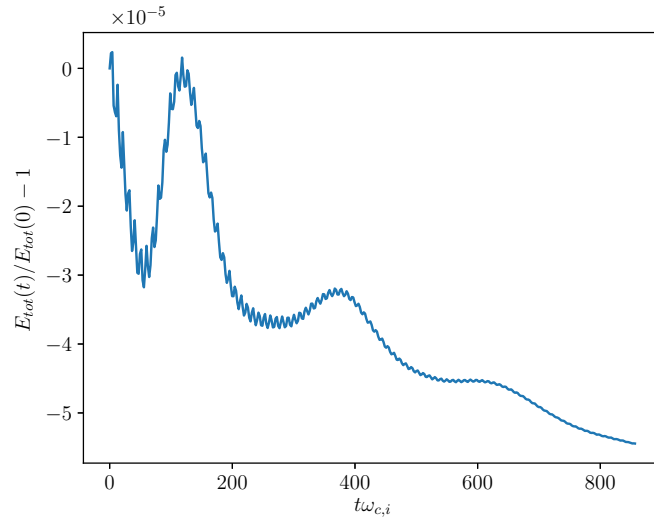


Figure 9: Evolution of total energy.

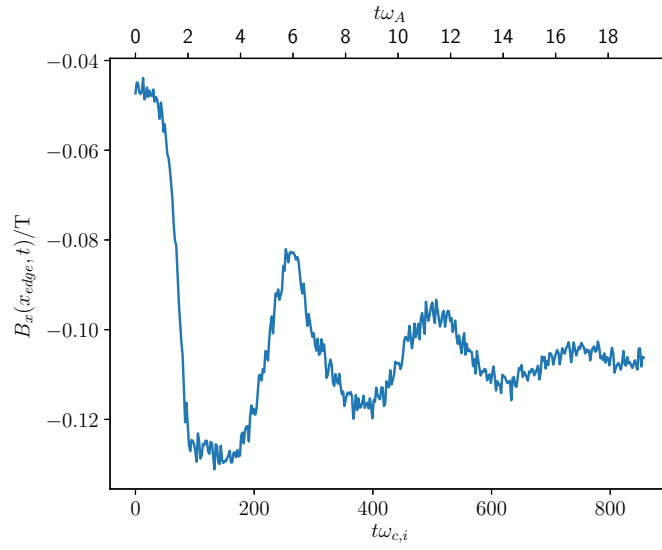


Figure 10: Evolution of $B_x(600\Delta x, 0, 512\Delta x)$.

we increase the plasma density to $n_0 = 1 \times 10^{20} \text{m}^{-3}$, and the rest of parameters are

$$\begin{aligned}
I_p &= 0.858 \text{MA}, \quad T_{e,0} = T_{i,0} = T_0 = 800 \text{eV}, \\
\Delta x &= 3.2 \times 10^{-3} \text{m}, \quad \Delta t = 0.5 \Delta x / c_n, \quad R_0 = 125 \Delta x, \\
c_n &= r_c c, \quad m_i = r_m m_e = 3.34 \times 10^{-27} \text{kg}, \\
J_{PF,i} &= 144.6 \text{kA}, \quad \text{for } 1 \leq i \leq 6, \\
J_{PF,7} &= J_{PF,8} = 448.3 \text{kA}, \quad J_{PF,9} = J_{PF,10} = 506.2 \text{kA}, \\
J_{PF,11} &= -367.6 \text{kA}, \quad J_{PF,12} = -448.3 \text{kA}.
\end{aligned}$$

Here r_m is the mass ratio between the deuterium and electron, c_n is the speed of light in the simulation and r_c is the ratio between c_n and the real speed of light in the vacuum c . For real plasmas, $r_m \approx 3672$ and $r_c = 1$. Limited by available computation power, we reduce r_m and r_c in some of the simulations. Such an approximation is valid because the low frequency ion motion is relatively independent from the mass of electron and the speed of light, as long as $r_m \gg 1$ and $(cr_c/v_A)^2 \gg 1$. In the present work, we take $r_m = 100$ and $r_c = 0.16$ to obtain long-term simulation results. Short-term results for $r_m = 300$, $r_c = 0.5$ and $r_m = 3672$, $r_c = 1$ (in this case $\Delta t = 0.1 \Delta x / c$) are also obtained for comparison. The simulation domain is a $192 \times 64 \times 256$ mesh, where perfect electric conductor is assumed at the boundaries in the x - and z -directions, and the periodic boundary is selected in y direction.

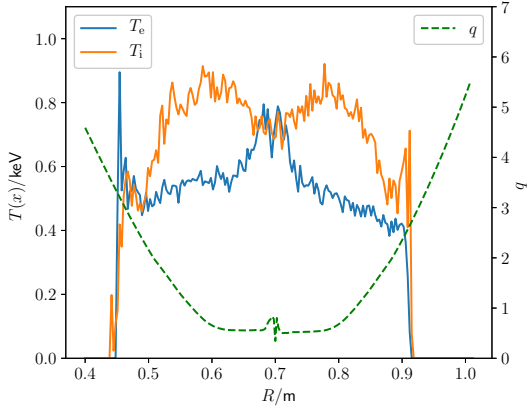
Because of the steep pressure gradient in the edge of the plasma, the threshold β_{crit} for ballooning mode instability is low. An estimated scaling for β_{crit} is [137],

$$\beta_{\text{crit}} = 0.6 \hat{s} / \left(\frac{2q^2 R_0}{L_p} \right),$$

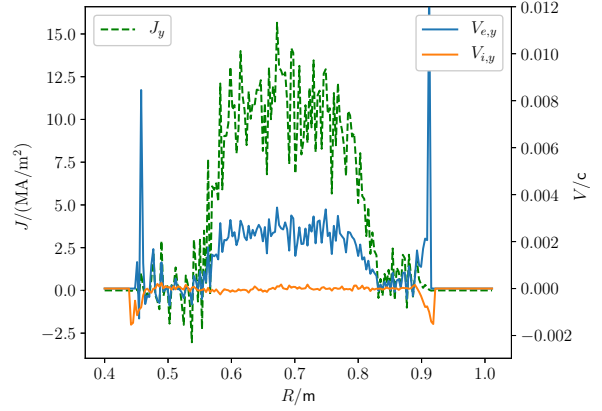
where \hat{s} is the magnetic shear and L_p is the pressure scaling length. For our simulated plasma, $\beta_{\text{crit}} \sim 1 \times 10^{-3}$ and $\beta \approx 3 \times 10^{-3}$. We expect to observe unstable KBM.

To obtain a self-consistent kinetic steady state, we first perform a simulation as described in Sec. III A and obtain the 2D kinetic steady state. The profiles of temperature, safety factor, number density, pressure, toroidal current and bulk velocity of this steady state at $z = 0.41 \text{m}$ are shown in Fig. 11.

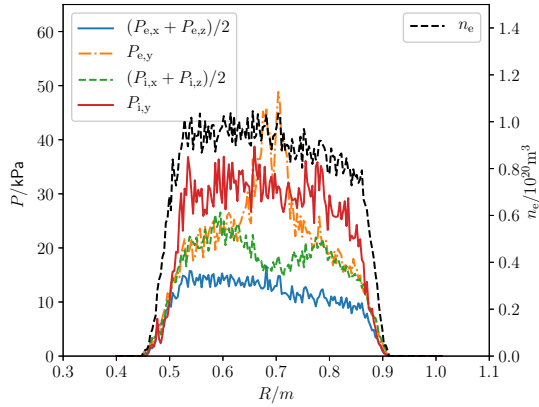
A random perturbation is then added in as the initial condition of the 6D simulation. The total simulation time is $t_a = 1.5 \times 10^6 \Delta t \approx 10000 \omega_{c,i}^{-1} \approx 5 \times 10^{-5} \text{s}$. For one such simulation



(a) Temperatures for electrons T_e and ions T_i , and the safety factor q



(b) Toroidal current J_y , toroidal bulk velocities for electrons $V_{e,y}$ and ions $V_{i,y}$



(c) Pressures for electrons P_e and ions P_i , and the number density of electron, here for both electrons and

ions it is found that $P_{i/e,x} \approx P_{i/e,z}$ so only

$$(P_{i/e,x} + P_{i/e,z})/2 \text{ is plotted.}$$

Figure 11: Profiles of the kinetic steady state at $z = 0.41\text{m}$.

it takes about 3×10^5 core-hours on the Tianhe 3 prototype cluster. The resulting mode structures of ion density for toroidal mode number $n = 1, 2, 3, 6, 10, 14, 18$ are shown in Figs. 12, 13 and 14 for $t\omega_{c,i} = 637, 1241$ and 9693 . It is clear that the unstable modes are triggered at the edge of the plasma, and the ballooning structure can be observed for modes with large n . The growth rate as a function of n is plotted in Fig. 15. For comparison, the

growth rate obtained using $r_c = 0.5$, $r_m = 300$ and $r_c = 1$, $r_m = 3672$ are also plotted. It is clear that the growth rate has little correlation with the reduction of r_c and r_m . Figure 15 shows that the growth rate increases with n , consistent with the early gyrokinetic simulation results obtained using the Kin-2DEM eigenvalue code [17, 18]. Because the number of grids in the toroidal direction is 64 and the width of interpolating function is 4 times the grid size, the results for modes with $n > 16$ may not be accurate. The results displayed here are thus preliminary. In the next step, we plan to perform a larger scale simulation with more realistic 2D equilibria to obtain improved accuracy.

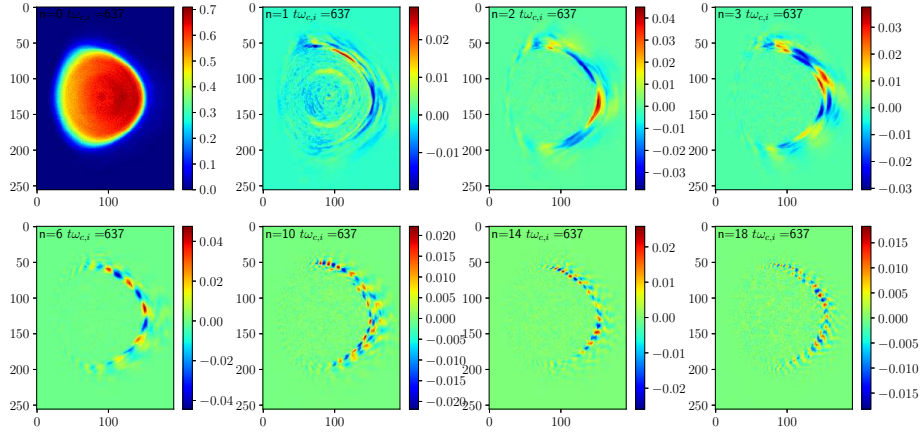


Figure 12: Mode structures of the electron density at $t = 637/\omega_{c,i} = 2.85a/v_{t,i}$.

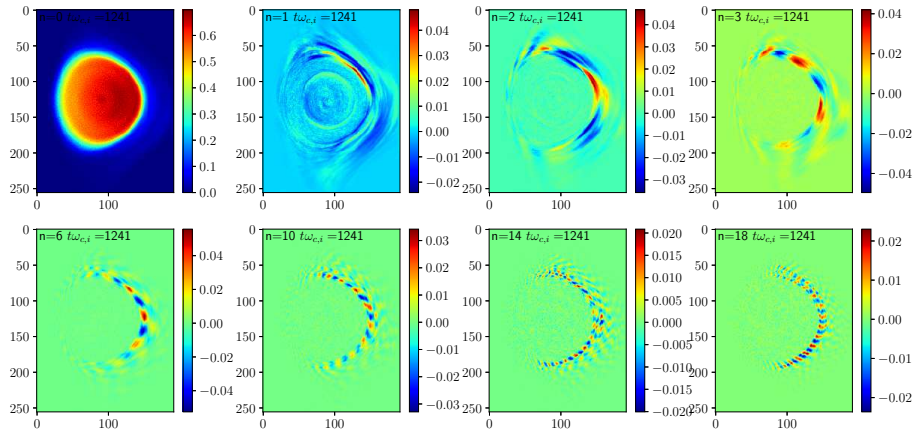


Figure 13: Mode structures of the electron density at $t = 1241/\omega_{c,i} = 5.55a/v_{t,i}$.

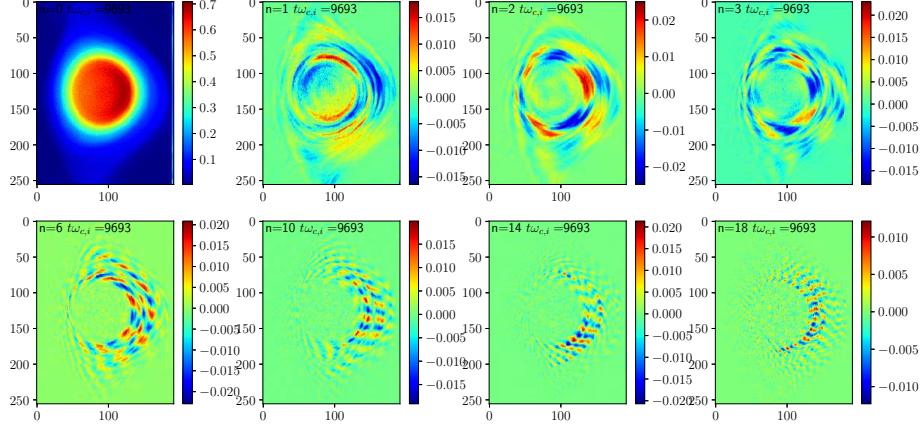


Figure 14: Mode structure of the electron density at $t = 9693/\omega_{c,i} = 43.35a/v_{t,i}$.

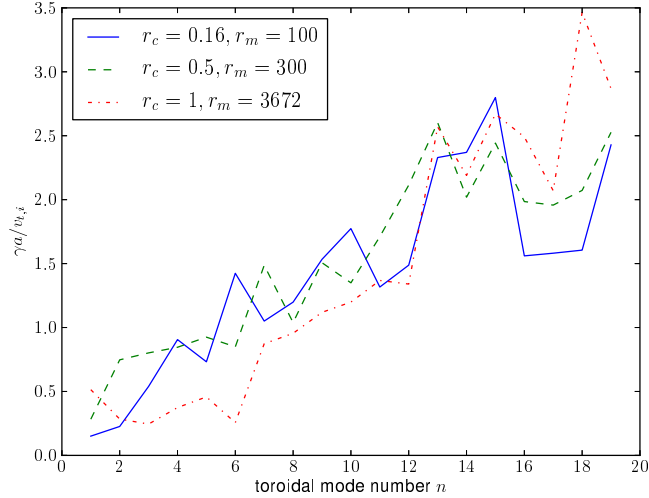
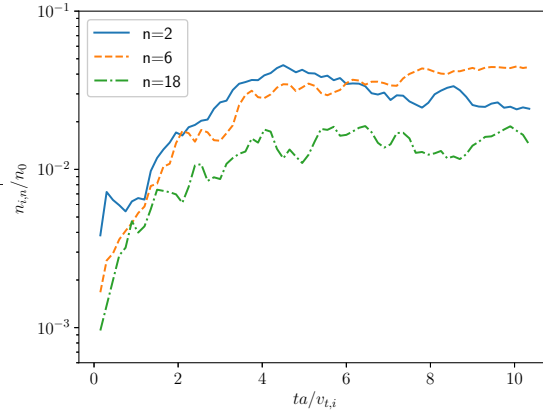
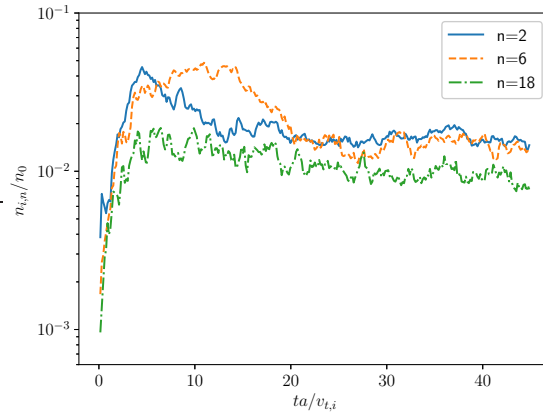


Figure 15: Growth rate as a function of toroidal mode number for different values of r_c and r_m .

The time-history of the mode amplitude is shown in Fig. 16. The unstable mode saturates approximately at $t \approx 5a/v_{t,i}$, and the saturation level is in the range of 2%. Recent nonlinear gyrokinetic simulation [19] suggested that the instability is saturated by the $E \times B$ zonal flow generated by the instability. To verify this mechanism in our 6D fully kinetic simulation, the toroidally averaged \mathbf{E} , $E \times B$ velocity and the measured phase velocity of the $n = 12$ mode at $z = 128\Delta x$ and $t = 8a/v_{t,i}$ are compared in Fig. 17. The $E \times B$ velocity at the edge correlates strongly with the phase velocity of the perturbation in terms of amplitude



(a) Short-term evolution.



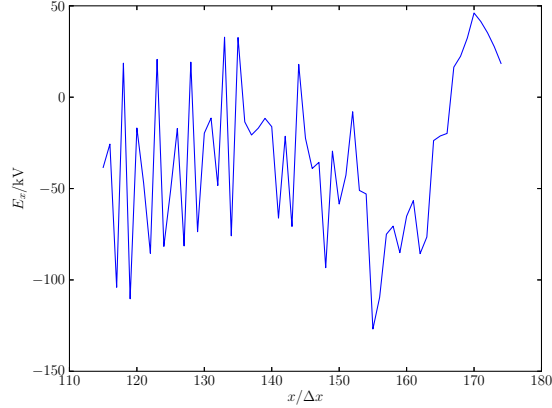
(b) Long-term evolution.

Figure 16: Time-history of ion densities for different toroidal mode number n .

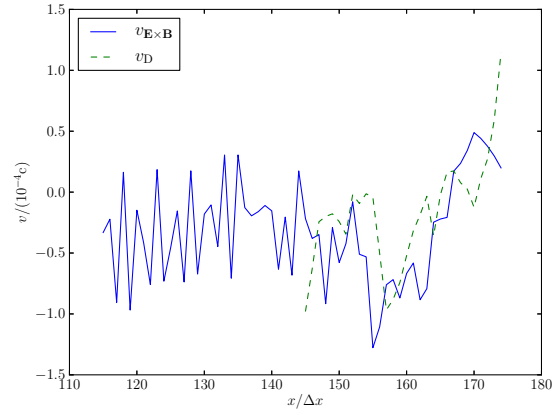
and profile. As a result, the $E \times B$ flow for the background plasma generated by instability interacts coherently with the mode structure, significantly modifies the space-time structure of the perturbation relative to the background plasma and reduces the drive of the instability. For this case simulated, the nonlinear saturation mechanism agrees qualitatively with the nonlinear gyrokinetic simulation [19].

IV. CONCLUSIONS

Even though 6D kinetic PIC method is a classical simulation tool for plasma physics, up to now it has not been applied to numerical studies of tokamak physics in spite of continuous



(a)



(b)

Figure 17: The toroidal averaged electric field in \mathbf{e}_x direction (a). The $E \times B$ velocity $v_{E \times B}$ and measured phase velocity v_D for the $n = 12$ mode in the \mathbf{e}_z direction at $z = 128\Delta x$ and $t = 8a/v_{t,i}$ (b) .

improvement [35–38, 41–43, 138–162]. In the present study, we have developed an explicit structure-preserving geometric PIC algorithm in curvilinear orthogonal meshes, in particular the cylindrical mesh, and apply it to carry out whole-device 6D kinetic simulation studies of tokamak physics. The work reported represents a further development of the structure-preserving geometric PIC algorithm [1–12], achieving the goal of practical applications in magnetic fusion research.

Along with its predecessors [1–12], the algorithm extends the symplectic integration method for finite dimensional canonical Hamiltonian systems developed since the 1980s [51–

55, 80–99], and preserves an infinite dimensional non-canonical symplectic structure of the particle-field systems. In addition, other important geometric structures and conservation laws, such as the gauge symmetry, the local charge conservation law [1, 2, 11, 116] and the local energy conservation law [10], are preserved exactly as well. These preserved structures and conservation laws improve the accuracy and fidelity of large-scale long-term simulations on modern computing hardware [33].

Through the whole-device 6D kinetic simulation, we numerically obtained a self-consistent kinetic steady state for fusion plasma in the tokamak geometry. It was found that the pressure tensor of the self-consistent kinetic steady state is diagonal, anisotropic in 3D, but isotropic in the poloidal plane. The steady state also includes a steady-state sub-sonic ion flow in the range of 10km/s, which agrees with previous experimental observations [13, 14] and theoretical calculations [15, 16]. Kinetic ballooning instability in the self-consistent kinetic steady state was successfully simulated. In the linear phase, it was found that high- n ballooning modes have larger growth rates than low- n global modes. In the nonlinear phase, the modes saturate approximately in 5 ion transit times at the 2% level by the $E \times B$ flow generated by the instability. These results qualitatively agrees with early [17, 18] and recent [19] simulations by electromagnetic gyrokinetic codes. In addition, compared with conventional gyrokinetic and reduced Braginskii Zeiler *et al.* [163], Xu *et al.* [164], Ricci *et al.* [165] fluid simulation methods, more physical effects, such as fully kinetic dynamics and the self-consistent radial electric field, are naturally included in the present method. These effects can be crucial for edge plasmas and will be investigated in the next step.

It worth mentioning that in the present work we can not directly control the 2D kinetic steady state because it is numerically evolved from a given initial condition. In the future, we plan to solve this problem by adopting MHD equilibrium solutions as the initial conditions. Because a MHD equilibrium should be at least close to a lowest order kinetic steady state, it is expected that a kinetic steady state can be obtained by a short time evolution.

The present work can be also extended to describe more complex physical processes in tokamak plasmas. For example, we can add energetic particles to investigate their interactions with the background plasma. An antenna can be also modeled as a current source to study the wave heating and current drive [166]. To simulate collision related physics, we can include Monte-Carlo Collision (MCC) [167] processes. It should be noted that due to the lack of marker particles in PIC simulations, the numerical collision frequency is usually

Physical quantity	Symbol(s)	Unit
Length	x, r, \dots	Δx
Velocity	\mathbf{v}	c_n
Mass	m_i	m_e
Time	t	$\Delta x/c_n$

Table II: Normalization for quantities.

larger than the real collision frequency of the plasma. More investigations are needed to determine the proper method to simulate collisions in the present scheme. Adding more physical effects to the geometric structure preserving PIC simulation framework will help us to better understand the tokamak physics. These topics will be addressed in the future study.

Appendix A: External magnetic field of the tokamak, initial particle loading, and the boundary setup

In this appendix we describe the setup of external magnetic field of the tokamak, initial particle loading, and the boundary setup for the simulation study. The normalization of quantities are listed in Table II.

The magnetic field is divided into three parts,

$$\mathbf{B}_{0,\text{init}} = \mathbf{B}_{0,p} + \mathbf{B}_{0,e} + \mathbf{B}_{0,t}, \quad (\text{A1})$$

where $\mathbf{B}_{0,e}$ is the external magnetic fields generated by poloidal coils, $\mathbf{B}_{0,t}$ is the magnetic field generated by toroidal coils, i.e.,

$$\mathbf{B}_{0,t} = \frac{B_0 R_0}{R}, \quad (\text{A2})$$

and they do not evolve with time. $\mathbf{B}_{0,p}$ is the magnetic field generated by the plasma current. The current \mathbf{j} and the vector potential \mathbf{A} are related by

$$\nabla \times (\nabla \times \mathbf{A}) = \mathbf{j}. \quad (\text{A3})$$

Initially, the current is in the y -direction and depends only on x and z . In the adopted

cylindrical coordinate (x, y, z) the line element is

$$ds^2 = (dx)^2 + \left(\frac{x + R_0}{R_0} dy \right)^2 + (dz)^2 , \quad (\text{A4})$$

and Eq. (A3) becomes

$$\frac{\partial^2}{\partial z^2} A_y(x, z) + \frac{\partial}{\partial x} \left(\frac{\partial}{(x + R_0) \partial x} (A_y(x, z) (x + R_0)) \right) = -j_y(x, z) , \quad (\text{A5})$$

$$\left(\frac{\partial^2}{\partial x^2} + \frac{\partial^2}{\partial z^2} \right) A_y^o(x, z) - \frac{1}{x + R_0} \frac{\partial}{\partial x} A_y^o(x, z) = -j_y^o(x, z) , \quad (\text{A6})$$

where

$$f^o(x, z) = f(x, z) \frac{x + R_0}{R_0} .$$

When $j_y(x, z) = I_0 \delta(x - x_0) \delta(z - z_0)$, which represents a coil current at (x_0, z_0) , Eq. (A6) can be solved using spherical harmonic expansion. However the convergence of the series is slow when $r_g = \sqrt{(x + r_0)^2 + (z - z_0)^2}$ approaches $x_0 + R_0$, the radius of the coil. We note that the second term in the left-hand-side of Eq. (A6) is negligible when $R_0 + x \gg B_z / (\partial B_z / \partial x)$. In this case, Eq. (A6) simplifies to

$$\left(\frac{\partial^2}{\partial x^2} + \frac{\partial^2}{\partial z^2} \right) A_y^o(x, z) = -j_y^o(x, z) , \quad (\text{A7})$$

which is a standard 2D Poisson equation. Its solution for the coil current at (x_0, z_0) with $I_0 = 1$ is

$$A_{y,PF}^o(x, z; x_0, z_0) = \frac{1}{4\pi} \log((x - x_0)^2 + (z - z_0)^2) . \quad (\text{A8})$$

Here, dimensionless variables have been used to simplify the notation. The total external vector potential generated by poloidal field coils is

$$A_{y,0,e}^o(x, z) = \sum_i J_{PF,i} A_{y,PF}^o(x, z; x_{PF,i}, z_{PF,i}) , \quad (\text{A9})$$

where the locations of poloidal field coils are displayed in Tab. III.

For $\mathbf{B}_{0,p}$ and the corresponding plasma current \mathbf{j}_0 , we first construct a vector potential $A_{y,0,p}$ and then use this potential to obtain $\mathbf{B}_{0,p}$ and \mathbf{j}_0 . The constructed $A_{y,0,p}$ is

$$A_{y,0,p}^o(x, z) = \begin{cases} -\frac{r^2 B_0}{2q_0 r_0} , & r \leq r_l , \\ -\frac{B_0}{q_0 r_0} \frac{9r^2 r_r + 6r_l^3 \log(r_l) + (-6 \log(r) - 5)r_l^3 - 4r^3}{18r_r - 18r_l} , & r_l < r \leq r_r , \\ -\frac{B_0}{q_0 r_0} \frac{6r_r^3 \log(r_r) + \log(r)(6r_r^3 - 6r_l^3) + 5r_r^3 + 6r_l^3 \log(r_l) - 5r_l^3}{18r_r - 18r_l} , & \text{otherwise,} \end{cases}$$

Coil number i	x/m	z/m	Coil number i	x/m	z/m
1	-0.05	0.4896	7	0.48	-0.1904
2	-0.05	0.3296	8	0.48	1.0096
3	-0.05	0.6496	9	0.62	0.0156
4	-0.05	0.1696	10	0.62	0.8036
5	-0.05	0.8096	11	0.08	1.0096
6	-0.05	0.0096	12	0.08	-0.1904

Table III: Locations of tokamak poloidal field coils.

where $r = \sqrt{(x - x_{\text{mid}})^2 + (z - z_{\text{mid}})^2}$, $x_{\text{mid}} = N_x/2$ and $z_{\text{mid}} = N_z/2$ are coordinates of the center of simulation domain, q_0 is the safety factor in the core of the plasma, $r_l = 0.454a = 0.1\text{m}$ and $r_r = 0.667a = 0.147\text{m}$ are two parameters that determine the current density distribution. The discrete magnetic fields are obtained by

$$\mathbf{B}_{J,0,p/e} = \text{curl}_d \mathbf{A}_{0,p/e}(i, j, k) , \quad (\text{A10})$$

and the discrete current density is obtained from

$$\mathbf{j}_{J,0,\text{all}} = \text{curl}_d^T \left((\mathbf{B}_{J,0,p} + \mathbf{B}_{J,0,e}) \left[(1 + i/r_0)^{-1}, 1 + i/r_0, (1 + i/r_0)^{-1} \right] \right) . \quad (\text{A11})$$

The final plasma current is chosen as

$$\mathbf{j}_{J,0} = \begin{cases} \mathbf{j}_{J,0,\text{all}} , & \text{when } r < r_r , \\ 0 , & \text{otherwise.} \end{cases} \quad (\text{A12})$$

Density and temperature are calculated from $A_{y,0}^o = A_{y,0,e}^o + A_{y,0,p}^o$. We introduce a reference function g_r defined as

$$g_r(x, z) = 1 - \begin{cases} 0 , & A_{y,0}^o(x, z) < A_{y,\text{min}}^o , \\ \frac{A_{y,0}^o(x, z) - A_{y,\text{min}}^o}{A_{y,\text{max}}^o - A_{y,\text{min}}^o} , & A_{y,\text{min}}^o \leq A_{y,0}^o(x, z) < A_{y,\text{max}}^o , \\ 1 , & A_{y,\text{max}}^o \leq A_{y,0}^o , \end{cases} \quad (\text{A13})$$

where

$$A_{y,\text{min}}^o = A_{y,0}^o(0.267N_x, 0.114N_z) , \quad (\text{A14})$$

$$A_{y,\text{max}}^o = A_{y,0}^o(0.488N_x, 0.369N_z) . \quad (\text{A15})$$

The initial density and temperature for electrons and ions are

$$n_e = n_i = n_{e,0} \left((g_r(x, z))^2 + 1 \right) \left(1 - g_r(x, z)^2 \right)^3, \quad (\text{A16})$$

$$T_e = T_i = T_{e,0} \left((g_r(x, z))^2 + 1 \right) \left(1 - g_r(x, z)^2 \right)^6. \quad (\text{A17})$$

In this work, ions are all deuterium ions, and the initial velocity distribution for each specie is Maxwellian with a flow velocity, i.e.,

$$f_{e/i,0}(\mathbf{x}, \mathbf{v}) = \frac{n_{e/i}(x, z)}{(2\pi T_{e/i}/m_{e/i})^{3/2}} \exp\left(-\frac{|\mathbf{v} + v_{e/i,y,0}(x, z) \mathbf{e}_y|^2}{2T_{e/i}/m_{e/i}}\right), \quad (\text{A18})$$

where

$$v_{e/i,y,0}(x, z) = \frac{j_{y,0}(x, z) m_{i/e}}{q_{e/i} (m_i - m_e) n_{e/i}(x, z)}. \quad (\text{A19})$$

The boundaries of the simulations are configured as follows. The boundaries at $x = 0$, $x = N_x \Delta x$, $z = 0$, and $z = N_z \Delta z$ are chosen to be perfect electric conductors for the electromagnetic fields. For particles, we introduce a thin slow-down layer,

$$\mathbf{L}_p = \left\{ (x, y, z) \mid 0 < x < 5\Delta x \quad \text{or} \quad 0 < z < 5\Delta z \quad \text{or} \right. \\ \left. (N_x - 5)\Delta x < x < N_x \Delta x \quad \text{or} \quad (N_z - 5)\Delta z < z < N_z \Delta z \right\}.$$

If a particle is inside \mathbf{L}_p at a time-step, its velocity \mathbf{v}_p will be reduced to $0.98\mathbf{v}_p$ at the end of this time-step, and the particle will be removed when \mathbf{v}_p is smaller than $1 \times 10^{-5}c$. Periodic boundaries for both particles and electromagnetic fields are adopted in the y -direction. The plasma is confined inside the last closed flux surface mostly, and the shape of plasma is not directly related to the simulation boundaries.

Appendix B: Explicit 2nd-order structure-preserving geometric PIC algorithm in the cylindrical mesh

In this appendix, we list the detailed update rule for the 2nd-order structure-preserving geometric PIC algorithm in the cylindrical mesh introduced in Sec. II E. It updates previous particle locations and discrete electromagnetic fields $\{\mathbf{x}_{sp,2l-2}, \mathbf{x}_{sp,2l-1}, \mathbf{E}_{J,l}, \mathbf{B}_{K,l}\}$ to the current ones $\{\mathbf{x}_{sp,2l}, \mathbf{x}_{sp,2l+1}, \mathbf{E}_{J,l+1}, \mathbf{B}_{K,l+1}\}$,

$$\begin{aligned}
x_{sp,2l} &= 2x_{sp,2l-1} - x_{sp,2l-2} + \Delta x^{-2} \left(2 \frac{q_s}{m_s} h^2 E_{x,1} \right) , \\
y_{sp,2l} &= \left(r_0^2 + 2r_0 x_{sp,2l} + x_{sp,2l}^2 \right)^{-1} \left((-2r_0 x_{sp,2l-2} - r_0^2 - x_{sp,2l-2}^2) y_{sp,2l-2} + \right. \\
&\quad \left. (2r_0^2 + 2r_0 x_{sp,2l-2} + x_{sp,2l-2}^2 + 2r_0 x_{sp,2l} + x_{sp,2l}^2) y_{sp,2l-1} \right) + \\
&\quad r_0^2 \left(\frac{q_s}{m_s} h (2E_{y,1} h - (B_{z,0,0,1,1,0} + B_{z,1,1,1,1,0})) \right) (\Delta y^2 r_0^2 + 2\Delta y^2 r_0 x_{sp,2l} + \Delta y^2 x_{sp,2l}^2)^{-1} , \\
z_{sp,2l} &= 2z_{sp,2l-1} - z_{sp,2l-2} + \\
&\quad \Delta z^{-2} \left(\frac{q_s}{m_s} h (2E_{z,1} h + (B_{y,0,0,1,1,0} - B_{x,0,0,0,1,1} - B_{x,1,2,1,1,1} + B_{y,1,1,1,1,0})) \right) , \\
z_{sp,2l+1} &= 2z_{sp,2l} - z_{sp,2l-1} , \\
y_{sp,2l+1} &= 2y_{sp,2l} - y_{sp,2l-1} + r_0^2 \left(h \frac{q_s}{m_s} (B_{x,1,2,2,2,2} + B_{x,1,2,2,1,2}) \right) (\Delta y^2 r_0^2 + 2\Delta y^2 r_0 x_{sp,2l} + \Delta y^2 x_{sp,2l}^2)^{-1} \\
x_{sp,2l+1} &= \Delta x^{-2} r_0^{-2} \left(-\Delta x^2 r_0^2 x_{sp,2l-1} + 2\Delta x^2 r_0^2 x_{sp,2l} + (\Delta y^2 r_0 + \Delta y^2 x_{sp,2l}) y_{sp,2l-1}^2 \right. \\
&\quad \left. + (-2\Delta y^2 r_0 - 2\Delta y^2 x_{sp,2l}) y_{sp,2l-1} y_{sp,2l} + (2\Delta y^2 r_0 + 2\Delta y^2 x_{sp,2l}) y_{sp,2l}^2 \right. \\
&\quad \left. + (-2\Delta y^2 r_0 - 2\Delta y^2 x_{sp,2l}) y_{sp,2l} y_{sp,2l+1} + (\Delta y^2 r_0 + \Delta y^2 x_{sp,2l}) y_{sp,2l+1}^2 \right) , \\
&\quad \left. + \Delta x^{-2} \left(-h \frac{q_s}{m_s} (B_{y,1,2,2,1,2} + B_{y,1,2,2,2,2} - B_{z,1,2,1,1,1} - B_{z,1,2,2,3,1}) \right) \right) ,
\end{aligned}$$

$$\begin{aligned}
\frac{1}{\mathbf{h}_{\sigma 1}(\mathbf{x}_J) \mathbf{h}_{\sigma 1}(\mathbf{x}_J)} \frac{\mathbf{E}_{J,l+1} - \mathbf{E}_{J,l}}{\Delta t} h_{\sigma 3}(\mathbf{x}_J) &= \sum_K \text{curl}_d^T{}_{J,K} \frac{h_{\sigma 3}(\mathbf{x}_J)}{\mathbf{h}_{\sigma 2}(\mathbf{x}_K) \mathbf{h}_{\sigma 2}(\mathbf{x}_K)} \mathbf{B}_{K,l} - \mathbf{j}_{J,l} , \\
\frac{\mathbf{B}_{K,l+1} - \mathbf{B}_{K,l}}{\Delta t} &= - \sum_J \text{curl}_{dK,J} \mathbf{E}_{J,l+1} ,
\end{aligned}$$

where

$$\begin{aligned}
h &= \Delta t/2, \\
\mathbf{B}_{t,i_1,i_2,i_3,i_4} &= \begin{bmatrix} B_{x,t,i_1,i_2,i_3,i_4} \\ B_{y,t,i_1,i_2,i_3,i_4} \\ B_{z,t,i_1,i_2,i_3,i_4} \end{bmatrix} = \int_{x_{i_4+1,sp,2l+i_4+1}}^{x_{i_4+1,sp,2l+i_4+1}+1} d\bar{x} \sum_J \mathbf{B}_{J,l+t-1} \\
&W_{\sigma_2 J} \left([x_{sp,2l+i_1}, y_{sp,2l+i_2}, z_{sp,2l+i_3}] + \mathbf{e}_{x_{i_4+1}} (\bar{x} - x_{i_4+1,sp,2l+i_4+1}) \right), \\
\mathbf{E}_1 &= \begin{bmatrix} E_{x,1} \\ E_{y,1} \\ E_{z,1} \end{bmatrix} = \sum_J \mathbf{E}_{J,l} W_{\sigma_1 J} (\mathbf{x}_{sp,2l-1}), \\
\mathbf{j}_{J,l} &= \frac{1}{\Delta t} \sum_{s,p} q_s \int_{C_{sp,2l-1,2l} \cup C_{sp,2l,2l+1}^*} W_{\sigma_1 J} (\mathbf{x}) d\mathbf{x}, \\
C_{sp,2l-1,2l} &= \{(x_{1,sp,2l-1} + \tau(x_{1,sp,2l} - x_{1,sp,2l-1}), x_{2,sp,2l-1}, x_{3,sp,2l-1}) | \tau \in [0, 1)\} \cup \\
&\{(x_{1,sp,2l}, x_{2,sp,2l-1} + \tau(x_{2,sp,2l} - x_{2,sp,2l-1}), x_{3,sp,2l-1}) | \tau \in [0, 1)\} \cup \\
&\{(x_{1,sp,2l}, x_{2,sp,2l}, x_{3,sp,2l-1} + \tau(x_{3,sp,2l} - x_{3,sp,2l-1})) | \tau \in [0, 1)\}, \\
C_{sp,2l,2l+1}^* &= \{(x_{1,sp,2l} + \tau(x_{1,sp,2l+1} - x_{1,sp,2l}), x_{2,sp,2l+1}, x_{3,sp,2l+1}) | \tau \in [0, 1)\} \cup \\
&\{(x_{1,sp,2l}, x_{2,sp,2l} + \tau(x_{2,sp,2l+1} - x_{2,sp,2l}), x_{3,sp,2l+1}) | \tau \in [0, 1)\} \cup \\
&\{(x_{1,sp,2l}, x_{2,sp,2l}, x_{3,sp,2l} + \tau(x_{3,sp,2l+1} - x_{3,sp,2l})) | \tau \in [0, 1)\}.
\end{aligned}$$

ACKNOWLEDGMENT

J. Xiao was supported by the the National MCF Energy R&D Program (2018YFE0304100), National Key Research and Development Program (2016YFA0400600, 2016YFA0400601 and 2016YFA0400602), and the National Natural Science Foundation of China (NSFC-11905220 and 11805273). J. Xiao developed the algorithm and the *SymPIC* code and carried out the simulation on Tianhe 3 prototype at the National Supercomputer Center in Tianjin and Sunway Taihulight in the National Supercomputer Center in Wuxi. H. Qin was supported by the U.S. Department of Energy (DE-AC02-09CH11466). H. Qin contributed to the

physical study of the self-consistent kinetic equilibrium and the kinetic ballooning modes.

- [1] J. Squire, H. Qin, and W. M. Tang, *Geometric Integration of the Vlasov-Maxwell System with a Variational Particle-in-cell Scheme*, Tech. Rep. PPPL-4748 (Princeton Plasma Physics Laboratory, 2012).
- [2] J. Squire, H. Qin, and W. M. Tang, *Physics of Plasmas* **19**, 084501 (2012).
- [3] J. Xiao, J. Liu, H. Qin, and Z. Yu, *Physics of Plasmas* **20**, 102517 (2013).
- [4] J. Xiao, H. Qin, J. Liu, Y. He, R. Zhang, and Y. Sun, *Physics of Plasmas* **22**, 112504 (2015).
- [5] J. Xiao, J. Liu, H. Qin, Z. Yu, and N. Xiang, *Physics of Plasmas* **22**, 092305 (2015).
- [6] Y. He, H. Qin, Y. Sun, J. Xiao, R. Zhang, and J. Liu, *Physics of Plasmas (1994-present)* **22**, 124503 (2015).
- [7] H. Qin, J. Liu, J. Xiao, R. Zhang, Y. He, Y. Wang, Y. Sun, J. W. Burby, L. Ellison, and Y. Zhou, *Nuclear Fusion* **56**, 014001 (2016).
- [8] Y. He, Y. Sun, H. Qin, and J. Liu, *Physics of Plasmas* **23**, 092108 (2016).
- [9] M. Kraus, K. Kormann, P. J. Morrison, and E. Sonnendrücker, *Journal of Plasma Physics* **83**, 905830401 (2017).
- [10] J. Xiao, H. Qin, J. Liu, and R. Zhang, *Physics of Plasmas* **24**, 062112 (2017).
- [11] J. Xiao, H. Qin, and J. Liu, *Plasma Science and Technology* **20**, 110501 (2018).
- [12] J. Xiao and H. Qin, *Nuclear Fusion* **59**, 106044 (2019).
- [13] A. Ince-Cushman, J. E. Rice, M. Reinke, M. Greenwald, G. Wallace, R. Parker, C. Fiore, J. W. Hughes, P. Bonoli, S. Shiraiwa, A. Hubbard, S. Wolfe, I. H. Hutchinson, E. Marmor, M. Bitter, J. Wilson, and K. Hill, *Physical Review Letters* **102**, 035002 (2009).
- [14] J. Rice, A. Ince-Cushman, P. Bonoli, M. Greenwald, J. Hughes, R. Parker, M. Reinke, G. Wallace, C. Fiore, R. Granetz, A. Hubbard, J. Irby, E. Marmor, S. Shiraiwa, S. Wolfe, S. Wukitch, M. Bitter, K. Hill, and J. Wilson, *Nuclear Fusion* **49**, 025004 (2009).
- [15] X. Guan, I. Y. Dodin, H. Qin, J. Liu, and N. J. Fisch, *Physics of Plasmas* **20**, 102105 (2013).
- [16] X. Guan, H. Qin, J. Liu, and N. J. Fisch, *Physics of Plasmas* **20**, 022502 (2013).
- [17] H. Qin, *Gyrokinetic Theory and Computational Methods for Electromagnetic Perturbations in Tokamaks*, Ph.D. thesis, Princeton University, Princeton, NJ 08540 (1998).
- [18] H. Qin, W. M. Tang, and G. Rewoldt, *Physics of Plasmas* **6**, 2544 (1999).

- [19] G. Dong, J. Bao, A. Bhattacharjee, and Z. Lin, *Physics of Plasmas* **26**, 010701 (2019).
- [20] J. M. Dawson, *Reviews of Modern Physics* **55**, 403 (1983).
- [21] R. W. Hockney and J. W. Eastwood, *Computer Simulation Using Particles* (CRC Press, 1988).
- [22] C. K. Birdsall and A. B. Langdon, *Plasma Physics via Computer Simulation* (IOP Publishing, 1991) p. 293.
- [23] K. S. Yee *et al.*, *IEEE Trans. Antennas Propag* **14**, 302 (1966).
- [24] J. Boris, in *Proceedings of the Fourth Conference on Numerical Simulation of Plasmas* (Naval Research Laboratory, Washington D. C., 1970) p. 3.
- [25] A. Stern, Y. Tong, M. Desbrun, and J. E. Marsden, in *Geometry, Mechanics, and Dynamics* (Springer, 2015) pp. 437–475.
- [26] H. Qin, S. Zhang, J. Xiao, J. Liu, Y. Sun, and W. M. Tang, *Physics of Plasmas (1994-present)* **20**, 084503 (2013).
- [27] Y. He, Y. Sun, J. Liu, and H. Qin, *Journal of Computational Physics* **281**, 135 (2015).
- [28] R. Zhang, J. Liu, H. Qin, Y. Wang, Y. He, and Y. Sun, *Physics of Plasmas (1994-present)* **22**, 044501 (2015).
- [29] C. Ellison, J. Burby, and H. Qin, *Journal of Computational Physics* **301**, 489 (2015).
- [30] Y. He, Y. Sun, J. Liu, and H. Qin, *Journal of Computational Physics* **305**, 172 (2016).
- [31] X. Tu, B. Zhu, Y. Tang, H. Qin, J. Liu, and R. Zhang, *Physics of Plasmas* **23**, 122514 (2016).
- [32] H. Ueda, Y. Omura, H. Matsumoto, and T. Okuzawa, *Computer physics communications* **79**, 249 (1994).
- [33] H. Fu, J. Liao, J. Yang, L. Wang, Z. Song, X. Huang, C. Yang, W. Xue, F. Liu, F. Qiao, *et al.*, *Science China Information Sciences* **59**, 072001 (2016).
- [34] P. J. Morrison, *Physics of Plasmas* **24**, 055502 (2017).
- [35] F. Holderied, S. Possanner, A. Ratnani, and X. Wang, *Journal of Computational Physics* **402**, 109108 (2020).
- [36] J. Xiao and H. Qin, “Structure-preserving geometric particle-in-cell algorithm suppresses finite-grid instability – comment on ”Finite grid instability and spectral fidelity of the electrostatic particle-in-cell algorithm” by Huang et al.” (2019), [arXiv:1904.00535v1](https://arxiv.org/abs/1904.00535v1).

- [37] Y. Li, Y. He, Y. Sun, J. Niesen, H. Qin, and J. Liu, [Journal of Computational Physics](#) **396**, 381 (2019).
- [38] Y. Li, Y. Sun, and N. Crouseilles, [Journal of Computational Physics](#) **405**, 109172 (2020).
- [39] E. Hirvijoki, K. Kormann, and F. Zonta, “Subcycling of particle orbits in variational, geometric electromagnetic particle-in-cell methods,” (2020), [arXiv:2002.10759v2](#).
- [40] B. Perse, K. Kormann, and E. Sonnendrücker, “Geometric particle-in-cell simulations of the vlasov–maxwell system in curvilinear coordinates,” (2020), [arXiv:2002.09386v1](#).
- [41] J. Zheng, J. Chen, F. Lu, J. Xiao, H. An, and L. Shen, [Plasma Physics and Controlled Fusion](#) **62**, 125020 (2020).
- [42] Z. Wang, H. Qin, B. Sturdevant, and C.-S. Chang, “Geometric electrostatic particle-in-cell algorithm on unstructured meshes,” (2020), [arXiv:2012.08587 \[physics.plasm-ph\]](#).
- [43] K. Kormann and E. Sonnendrücker, [Journal of Computational Physics](#) **425**, 109890 (2021).
- [44] Z. Lin, T. S. Hahm, W. Lee, W. M. Tang, and R. B. White, [Science](#) **281**, 1835 (1998).
- [45] L. Zebin, S. Guoya, I. Holod, X. Yong, Z. Wenlu, and L. Zhihong, [Plasma Science and Technology](#) **15**, 499 (2013).
- [46] S. Ku, C.-S. Chang, M. Adams, J. Cummings, F. Hinton, D. Keyes, S. Klasky, W. Lee, Z. Lin, S. Parker, *et al.*, [Journal of Physics: Conference Series](#) **46**, 87 (2006).
- [47] C.-S. Chang, S. Ku, P. Diamond, Z. Lin, S. Parker, T. Hahm, and N. Samatova, [Physics of Plasmas](#) **16**, 056108 (2009).
- [48] Y. Chen and S. E. Parker, [Journal of Computational Physics](#) **189**, 463 (2003).
- [49] Y. Chen and S. E. Parker, [Journal of Computational Physics](#) **220**, 839 (2007).
- [50] E. Wang, X. Xu, J. Candy, R. Groebner, P. Snyder, Y. Chen, S. Parker, W. Wan, G. Lu, and J. Dong, [Nuclear Fusion](#) **52**, 103015 (2012).
- [51] T. Lee, [Phys. Lett. B](#) **122**, 217 (1983).
- [52] T. Lee, [J. Statist. Phys.](#) **46**, 843 (1987).
- [53] A. P. Veselov, [Funkc. Anal. Priloz.](#) **22**, 1 (1988).
- [54] J. E. Marsden and M. West, [Acta Numer.](#) **10**, 357 (2001).
- [55] G. Han-Ying, L. Yu-Qi, W. Ke, and W. Shi-Kun, [Communications in Theoretical Physics](#) **37**, 257 (2002).
- [56] H. Qin, [Scientific Reports](#) **10**, 19329 (2020).

- [57] I. Hutchinson, R. Boivin, F. Bombarda, P. Bonoli, S. Fairfax, C. Fiore, J. Goetz, S. Golovato, R. Granetz, M. Greenwald, *et al.*, [Physics of Plasmas](#) **1**, 1511 (1994).
- [58] M. Greenwald, R. Boivin, F. Bombarda, P. Bonoli, C. Fiore, D. Garnier, J. Goetz, S. Golovato, M. Graf, R. Granetz, *et al.*, [Nuclear Fusion](#) **37**, 793 (1997).
- [59] J. Xiao, H. Qin, P. J. Morrison, J. Liu, Z. Yu, R. Zhang, and Y. He, [Physics of Plasmas \(1994-present\)](#) **23**, 112107 (2016).
- [60] Y. Zhou, H. Qin, J. Burby, and A. Bhattacharjee, [Physics of Plasmas \(1994-present\)](#) **21**, 102109 (2014).
- [61] Y. Zhou, Y.-M. Huang, H. Qin, and A. Bhattacharjee, [Phys. Rev. E](#) **93**, 023205 (2016).
- [62] Y. Zhou, *Variational Integration for Ideal Magnetohydrodynamics and Formation of Current Singularities*, [Ph.D. thesis](#), Princeton University (2017).
- [63] Y. Zhou, Y.-M. Huang, H. Qin, and A. Bhattacharjee, [The Astrophysical Journal](#) **852**, 3 (2017).
- [64] J. W. Burby and C. Tronci, [Plasma Physics and Controlled Fusion](#) **59**, 045013 (2017).
- [65] Q. Chen, H. Qin, J. Liu, J. Xiao, R. Zhang, Y. He, and Y. Wang, [Journal of Computational Physics](#) **349**, 441 (2017).
- [66] Y. Shi, N. J. Fisch, and H. Qin, [Physical Review A](#) **94**, 012124 (2016).
- [67] Y. Shi, J. Xiao, H. Qin, and N. J. Fisch, [Physical Review E](#) **97**, 053206 (2018).
- [68] Y. Shi, *Plasma Physics in Strong Field Regimes*, [Ph.D. thesis](#), Princeton University (2018).
- [69] Y. Shi, H. Qin, and N. J. Fisch, “Plasma physics in strong-field regimes: theories and simulations,” (2020), [arXiv:2012.15363 \[physics.plasm-ph\]](#).
- [70] Q. Chen and J. Xiao, “Gauge and Poincaré invariant canonical symplectic algorithms for real-time lattice strong-field quantum electrodynamics,” (2019), [arXiv:1910.09215v2](#).
- [71] E. Hirvijoki, M. Kraus, and J. W. Burby, “Metriplectic particle-in-cell integrators for the landau collision operator,” (2018), [arXiv:1802.05263](#).
- [72] A. N. Hirani, *Discrete Exterior Calculus*, [Ph.D. thesis](#), California Institute of Technology (2003).
- [73] M. Desbrun, A. N. Hirani, M. Leok, and J. E. Marsden, “Discrete exterior calculus,” (2005), [arXiv:math/0508341](#).
- [74] H. Whitney, *Geometric Integration Theory* (Princeton University Press, 1957).
- [75] P. J. Morrison, [Physics Letters A](#) **80**, 383 (1980).

- [76] J. E. Marsden and A. Weinstein, *Physica D: Nonlinear Phenomena* **4**, 394 (1982).
- [77] A. Weinstein and P. J. Morrison, *Physics Letters A* **86**, 235 (1981).
- [78] J. W. Burby, *Physics of Plasmas* **24**, 032101 (2017).
- [79] Z. R. Iwinski and L. A. Turski, *Letters in Applied and Engineering Sciences* **4**, 179 (1976).
- [80] R. Devogelaere, *Methods of Integration Which Preserve the Contact Transformation Property of the Hamilton Equations*, Tech. Rep. (University of Notre Dame, 1956).
- [81] R. D. Ruth, *IEEE Trans. Nucl. Sci* **30**, 2669 (1983).
- [82] K. Feng, in *the Proceedings of 1984 Beijing Symposium on Differential Geometry and Differential Equations*, edited by K. Feng (Science Press, 1985) pp. 42–58.
- [83] K. Feng, *J. Comput. Maths.* **4**, 279 (1986).
- [84] J. M. Sanz-Serna, *BIT* **28**, 877 (1988).
- [85] H. Yoshida, *Physics Letters A* **150**, 262 (1990).
- [86] E. Forest and R. D. Ruth, *Physica D* **43**, 105 (1990).
- [87] P. J. Channell and C. Scovel, *Nonlinearity* **3**, 231 (1990).
- [88] J. Candy and W. Rozmus, *Journal of Computational Physics* **92**, 230 (1991).
- [89] Y.-F. Tang, *Computers & Mathematics with Applications* **25**, 83 (1993).
- [90] J. M. Sanz-Serna and M. P. Calvo, *Numerical Hamiltonian Problems* (Chapman and Hall, London, 1994).
- [91] Z. Shang, *Journal of Computational Mathematics* **2**, 265 (1994).
- [92] F. Kang and S. Zai-jiu, *Numerische Mathematik* **71**, 451 (1995).
- [93] Z. Shang, *Numerische Mathematik* **83**, 477 (1999).
- [94] E. Hairer, C. Lubich, and G. Wanner, *Geometric Numerical Integration: Structure-Preserving Algorithms for Ordinary Differential Equations* (Springer, New York, 2002).
- [95] J. Hong and M. Z. Qin, *Applied Mathematics Letters* **15**, 1005 (2002).
- [96] Z. jiu Shang, *Journal of Physics A: Mathematical and General* **39**, 5601 (2006).
- [97] K. Feng and M. Qin, *Symplectic Geometric Algorithms for Hamiltonian Systems* (Springer-Verlag, 2010).
- [98] R. Zhang, H. Qin, Y. Tang, J. Liu, Y. He, and J. Xiao, *Physical Review E* **94**, 013205 (2016).
- [99] M. Tao, *Journal of Computational Physics* **327**, 245 (2016).
- [100] H. Qin and X. Guan, *Physical Review Letters* **100**, 035006 (2008).
- [101] H. Qin, X. Guan, and W. M. Tang, *Physics of Plasmas (1994-present)* **16**, 042510 (2009).

- [102] J. Squire, H. Qin, and W. M. Tang, [Physics of Plasmas](#) **19**, 052501 (2012).
- [103] R. Zhang, J. Liu, Y. Tang, H. Qin, J. Xiao, and B. Zhu, [Physics of Plasmas \(1994-present\)](#) **21**, 032504 (2014).
- [104] C. L. Ellison, J. M. Finn, H. Qin, and W. M. Tang, [Plasma Physics and Controlled Fusion](#) **57**, 054007 (2015).
- [105] J. Burby and C. Ellison, [Physics of Plasmas](#) **24**, 110703 (2017).
- [106] M. Kraus, “Projected variational integrators for degenerate lagrangian systems,” (2017), [arXiv:1708.07356v1](#).
- [107] C. L. Ellison, J. M. Finn, J. W. Burby, M. Kraus, H. Qin, and W. M. Tang, [Physics of Plasmas](#) **25**, 052502 (2018).
- [108] C. L. Ellison, *Development of Multistep and Degenerate Variational Integrators for Applications in Plasma Physics*, [Ph.D. thesis](#), Princeton University (2016).
- [109] Y. He, Z. Zhou, Y. Sun, J. Liu, and H. Qin, [Physics Letters A](#) **381**, 568 (2017).
- [110] Z. Zhou, Y. He, Y. Sun, J. Liu, and H. Qin, [Physics of Plasmas](#) **24**, 052507 (2017).
- [111] J. Xiao and H. Qin, [Computer Physics Communications](#) **241**, 19 (2019).
- [112] Y. Shi, Y. Sun, Y. He, H. Qin, and J. Liu, [Numerical Algorithms](#) **81**, 1295 (2019).
- [113] J. Xiao and H. Qin, “Slow manifolds of classical Pauli particle enable structure-preserving geometric algorithms for guiding center dynamics,” (2020), [arXiv:2006.03818v1 \[physics.plasm-ph\]](#).
- [114] N. Crouseilles, L. Einkemmer, and E. Faou, [Journal of Computational Physics](#) **283**, 224 (2015).
- [115] H. Qin, Y. He, R. Zhang, J. Liu, J. Xiao, and Y. Wang, [Journal of Computational Physics](#) **297**, 721 (2015).
- [116] A. S. Glasser and H. Qin, [Journal of Plasma Physics](#) **86**, 835860303 (2020).
- [117] A. S. Glasser and H. Qin, “Restoring Poincaré symmetry to the lattice,” (2019), [arXiv:1902.04396v1](#).
- [118] A. S. Glasser and H. Qin, “Lifting spacetime’s Poincaré symmetries,” (2019), [arXiv:1902.04395v1](#).
- [119] J. Xiao, H. Qin, Y. Shi, J. Liu, and R. Zhang, [Physics Letters A](#) **383**, 808 (2019).
- [120] W. Tang, J. Connor, and R. Hastie, [Nuclear Fusion](#) **20**, 1439 (1980).

- [121] P. Lauber, S. Günter, A. Könies, and S. Pinches, [Journal of Computational Physics](#) **226**, 447 (2007).
- [122] T. S. Hahm, [Physics of Fluids](#) **31**, 2670 (1988).
- [123] A. Brizard, [Journal of Plasma Physics](#) **41**, 541 (1989).
- [124] H. Qin, W. M. Tang, and G. Rewoldt, [Physics of Plasmas](#) **5**, 1035 (1998).
- [125] H. Qin, W. M. Tang, W. W. Lee, and G. Rewoldt, [Physics of Plasmas](#) **6**, 1575 (1999).
- [126] H. Qin, W. Tang, and G. Rewoldt, [Physics of Plasmas](#) **6**, 2544 (1999).
- [127] H. Qin, W. M. Tang, and W. W. Lee, [Physics of Plasmas](#) **7**, 4433 (2000).
- [128] H. Sugama, [Physics of Plasmas](#) **7**, 466 (2000).
- [129] H. Qin and W. M. Tang, [Physics of Plasmas](#) **11**, 1052 (2004).
- [130] H. Qin, [Fields Institute Communications](#) **46**, 171 (2005).
- [131] H. Qin, R. H. Cohen, W. M. Nevins, and X. Q. Xu, [Physics of Plasmas](#) **14**, 056110 (2007).
- [132] J. Burby, A. Brizard, P. Morrison, and H. Qin, [Physics Letters A](#) **379**, 2073 (2015).
- [133] J. W. Burby, *Chasing Hamiltonian Structure in Gyrokinetic Theory*, Ph.D. thesis, Princeton University (2015).
- [134] J. W. Burby and A. Brizard, [Physics Letters A](#) **383**, 2172 (2019).
- [135] W. Wan, S. E. Parker, Y. Chen, Z. Yan, R. J. Groebner, and P. B. Snyder, [Physical review letters](#) **109**, 185004 (2012).
- [136] W. Wan, S. E. Parker, Y. Chen, R. J. Groebner, Z. Yan, A. Y. Pankin, and S. E. Kruger, [Physics of Plasmas](#) **20**, 055902 (2013).
- [137] M. J. Pueschel, M. Kammerer, and F. Jenko, [Physics of Plasmas](#) **15**, 102310 (2008).
- [138] H. Okuda, [Journal of Computational Physics](#) **10**, 475 (1972).
- [139] B. I. Cohen, A. B. Langdon, and A. Friedman, [Journal of Computational Physics](#) **46**, 15 (1982).
- [140] A. B. Langdon, B. I. Cohen, and A. Friedman, [Journal of Computational Physics](#) **51**, 107 (1983).
- [141] B. I. Cohen, A. B. Langdon, D. W. Hewett, and R. J. Procassini, [Journal of Computational Physics](#) **81**, 151 (1989).
- [142] P. C. Liewer and V. K. Decyk, [Journal of Computational Physics](#) **85**, 302 (1989).
- [143] A. Friedman, S. E. Parker, S. L. Ray, and C. K. Birdsall, [Journal of Computational Physics](#) **96**, 54 (1991).

- [144] J. W. Eastwood, [Computer Physics Communications](#) **64**, 252 (1991).
- [145] J. Cary and I. Dexas, [Journal of Computational Physics](#) **107**, 98 (1993).
- [146] J. Villasenor and O. Buneman, [Computer Physics Communications](#) **69**, 306 (1992).
- [147] H. Qin, R. C. Davidson, and W. W. Lee, [Physical Review Special Topics - Accelerators and Beams](#) **3**, 084401 (2000).
- [148] H. Qin, R. C. Davidson, and W. W. Lee, [Physics Letters A](#) **272**, 389 (2000).
- [149] H. Qin, R. C. Davidson, W. W. Lee, and R. Kolesnikov, [Nuclear Instruments and Methods in Physics Research Section A](#) **464**, 477 (2001).
- [150] R. C. Davidson and H. Qin, [Physics of Intense Charged Particle Beams in High Energy Accelerators](#) (Imperial College Press and World Scientific, Singapore, 2001).
- [151] T. Z. Esirkepov, [Computer Physics Communications](#) **135**, 144 (2001).
- [152] J.-L. Vay, P. Colella, P. McCorquodale, B. van Straalen, A. Friedman, and D. P. Grote, [Laser and Particle Beams](#) **20**, 569 (2002).
- [153] C. Nieter and J. R. Cary, [Journal of Computational Physics](#) **196**, 448 (2004).
- [154] C. Huang, V. K. Decyk, C. Ren, M. Zhou, W. Lu, W. B. Mori, J. H. Cooley, T. M. Antonsen, and T. Katsouleas, [Journal of Computational Physics](#) **217**, 658 (2006).
- [155] N. Crouseilles, M. Mehrenberger, and E. Sonnendrucker, [Journal of Computational Physics](#) **229**, 1927 (2007).
- [156] G. Chen, L. Chacón, and D. C. Barnes, [Journal of Computational Physics](#) **230**, 7018 (2011).
- [157] L. Chacón, G. Chen, and D. Barnes, [Journal of Computational Physics](#) **233**, 1 (2013).
- [158] E. Evstatiev and B. Shadwick, [Journal of Computational Physics](#) **245**, 376 (2013).
- [159] B. A. Shadwick, A. B. Stamm, and E. G. Evstatiev, [Physics of Plasmas](#) **21**, 055708 (2014).
- [160] H. Moon, F. L. Teixeira, and Y. A. Omelchenko, [Computer Physics Communications](#) **194**, 43 (2015).
- [161] C.-K. Huang, Y. Zeng, Y. Wang, M. Meyers, S. Yi, and B. Albright, [Computer Physics Communications](#) **207**, 123 (2016).
- [162] S. D. Webb, [Plasma Physics and Controlled Fusion](#) **58**, 034007 (2016).
- [163] A. Zeiler, J. Drake, and B. Rogers, [Physics of Plasmas](#) **4**, 2134 (1997).
- [164] X. Q. Xu, B. Dudson, P. B. Snyder, M. V. Umansky, and H. Wilson, [Phys. Rev. Lett.](#) **105**, 175005 (2010).

- [165] P. Ricci, F. Halpern, S. Jolliet, J. Loizu, A. Masetto, A. Fasoli, I. Furno, and C. Theiler, [Plasma Physics and Controlled Fusion](#) **54**, 124047 (2012).
- [166] J. Zheng, J. Chen, F. Lu, J. Xiao, H. An, and L. Shen, [Plasma Physics and Controlled Fusion](#) **62**, 125020 (2020).
- [167] C. K. Birdsall, [IEEE Transactions on plasma science](#) **19**, 65 (1991).